Correspondence to:

W. Panasawatwong,
rung.panasawatwong@colostate.edu

A Climatology of Extreme Convective Storms in Tropical and Subtropical East Asia and Their Ingredients for Heavy Rainfall as Seen by TRMM

Warittha Panasawatwong[1] (ID)**, Kristen L. Rasmussen**[1] (ID)**, and Michael M. Bell**[1] (ID)

[1]Department of Atmospheric Science, Colorado State University, Fort Collins, CO, USA

Abstract Heavy rainfall is a challenge to forecast due to the variety of rainfall intensities and durations across a wide spectrum of high-impact storm types. In this study, we analyze extreme storms in Tropical and Subtropical East Asia, a moisture-rich environment with complex terrain and oceanic regions. The Tropical Rainfall Measuring Mission's Precipitation Radar is utilized to characterize the frequency and rainfall intensity of four extreme storm types. Extreme storms producing heavy precipitation are categorized into four types: deep convective cores (DCCs), deepwide convective cores (DWCCs), wide convective cores (WCCs), and broad stratiforms regions (BSRs). DCCs and DWCCs occur more frequently and produce stronger rain intensities over land compared to those over ocean. However, WCCs and BSRs occur more frequently over oceans, especially in association with the Meiyu front season and climatological progression in the northern subregions. Although the Convective Cores show higher rain intensities than the BSRs, they show lower volumetric rain rate due to their comparatively smaller horizontal area. An ingredients-based framework is applied to find key similarities across the different heavy rainfall-producing storms near Taiwan using ERA5 reanalysis. The analysis shows that the broader systems (i.e., WCCs and BSRs) are associated with larger in area and longer timescales of vertical moisture flux and low-level wind shear that support the development of the horizontally large, organized storms. Smaller DCCs do not show strong vertical moisture flux on the spatial scales resolved by the reanalysis, suggesting their more local nature and less meso- or synoptic scale support.

Plain Language Summary Heavy rainfall is a challenge to forecast due to the variety of rainfall intensities and durations across a wide spectrum of high-impact storm types. In this study, we analyze extreme storms in Tropical and Subtropical East Asia (TSEA), a moisture-rich environment with complex terrain and oceanic regions. Observations from the first satellite precipitation radar are used to characterize the nature of extreme storms. Results show that deep convective storms occur more frequently over land, while the wide convective storms and the broad stratiform regions occur more frequently over oceans, especially in association with the Meiyu front (pre-East Asian monsoon season) in northern TSEA. Broad stratiform regions can produce a larger total rainfall amount compared to the convective rain categories because of larger areas. A goal of this study is to identify similar key ingredients across different extreme storm types near Taiwan. Analysis shows that the broader storms are associated with moisture in larger areas and on longer timescales, and also low-level wind shear that supports the development of the large, organized storms. Smaller deep convective storms do not show strong moisture signals in coarse-scale environmental analysis, suggesting that this storm type might need more small-scale moisture support.

1. Introduction

Heavy rainfall is a high-impact weather phenomenon that disrupts the economy and impacts human life around the world every year. In the US, flooding is the second most deadly weather-related natural disaster (Ashley & Ashley, 2008). The contiguous US also broke the 12-month record of highest precipitation in July 2018–June 2019, and the top six of the wettest 12-month periods have been in the past 10 years (Leslie, 2019). The US has also recently seen multiple state rainfall records broken due to tropical cyclones (TCs) such as Hurricane Harvey (Brauer et al., 2020; DeHart & Bell, 2020) and Hurricane Lane (Nugent et al., 2020). Rainfall systems that produce heavy rainfall vary in their intensity and duration across a wide spectrum of storm types, such that an extreme rainfall event needs to have high intensity, long duration, or both. Given the wide variety of rainfall systems that can produce heavy rainfall, it is very challenging to predict these events using numerical weather prediction (NWP) models (Sukovich et al., 2014).

In addition to having a large impact in the current climate, heavy rainfall is expected to increase in a future warmer climate given that the increasing global-mean temperature will increase the amount of water vapor in the atmosphere by 7% per degree Celsius according to the Clausius-Clapeyron relation. Climate change may lead to an increase in precipitation and probability for floods with extreme rain characteristics (Dougherty & Rasmussen, 2020, 2021). For example, the precipitation from the intense convective storms and the chance for flash floods over the Mississippi river basin is expected to increase in the warming future (Dougherty & Rasmussen, 2021). In addition, an overall increase in rainfall and flooding associated with TCs is expected to increase (Gutmann et al., 2018; Knutson et al., 2020). In the US, the total damage may increase in the future due to the growing population in coastal cities impacted by TCs (Klotzbach et al., 2018).

To investigate the common factors of different extreme rainfall events, Doswell et al. (1996) proposed the ingredients-based framework for understanding rainfall intensity (I) and duration (D) separately, such that

$$P = I \times D, \tag{1}$$

where P is the net accumulated precipitation. The Intensity can be represented as

$$I = Ewq, \tag{2}$$

where E is precipitation efficiency, w is vertical velocity, and q is the water vapor mixing ratio. The duration is the amount of time that a storm is present over an observing point,

$$D = L/C \tag{3}$$

where L is the length scale of the storm, and C is the horizontal velocity of the storm along that length scale. This framework can be used to evaluate the spectrum of storms producing heavy precipitation from NWP models as well as from observations, making it a useful framework to improve our understanding of heavy rainfall.

A key ingredient for heavy rainfall production is moisture, as represented by the water vapor mixing ratio in Doswell's framework (Equation 2). In many arid or continental regions, floods are often the result of an unusually high moisture air mass being advected into the area. These anomalous high moisture environments may lead to an under-prediction of heavy rainfall from NWP models. For example, the 2013 Front Range flood in Colorado was not well forecasted because of the underestimated high moisture air with a tropical characteristic located east of the Rocky Mountains for an extended period of time, leading to a significant underestimate of rainfall from both NWP models and radar-estimated rainfall (Gochis et al., 2015). The 2010 Leh India and Pakistan floods (Houze et al., 2011; Rasmussen & Houze, 2012) and other extreme floods in Pakistan (Rasmussen et al., 2015) were also the result of the combination of anomalous high moisture air masses that were orographically lifted along the foothills of the Himalayas.

In contrast to arid environments, tropical oceanic regions frequently have abundant moisture available for rainfall production. The presence of ample water vapor is only one necessary but insufficient condition for heavy rain. For example, in Tropical and Subtropical East Asia (TSEA) during the spring and summer months, the southwest monsoonal flow provides an ample supply of water vapor from the deep tropics into the subtropics. In these moisture-rich environments, the variability in the other ingredients in Doswell's framework take on a greater role. In the TSEA region, the Meiyu front associated with the East Asian monsoon often provides a focal point for vertical motion over a large area and long duration, leading to frequent extreme rainfall and extreme storms to the region from May to July (Akiyama, 1973; Ding & Chan, 2005; Sampe & Xie, 2010). In addition, TCs frequently pass through this region in July-August, bringing additional extreme rainfall events into the region (C.-S. Chen et al., 2007; Wu et al., 2017).

A campaign called the Prediction of Rainfall Extremes Campaign in the Pacific (PRECIP, details can be found at http://precip.org/) will study the processes producing heavy rainfall in the moisture-rich environment of TSEA. The PRECIP study region is focused on Taiwan and southern Japan where heavy rain events are common due to the abundant monsoon moisture and presence of the Meiyu front, TCs, land-sea contrasts, and complex terrain. In preparation for the PRECIP field campaign, it is important to have a broader understanding of the nature of precipitating systems with extreme characteristics in the TSEA. In this study, we utilize observations from the Tropical Rainfall Measuring Mission (TRMM) satellite's Precipitation Radar (PR) that allows us to observe a wide spectrum of storms over the entire TSEA region over a multi-year record from 1998 to 2013. TRMM

Figure 1. Geographical location of Tropical and Subtropical East Asia and its subregions during May–September. Blue boxes mark sea-only subregions. Black boxes mark land-only subregions and land-and-sea subregion (namely Taiwan).

PR observations have provided unprecedented information to study the nature of precipitating systems globally (Houze et al., 2015b; Zipser et al., 2006), including rainfall associated with the Indian summer monsoon (Houze et al., 2007; Romatschke et al., 2010), floods in India and Pakistan (Houze et al., 2011; Rasmussen & Houze, 2012; Rasmussen et al., 2015), and deep convection east of the Andes in subtropical South America (Rasmussen & Houze, 2011, 2016; Rasmussen et al., 2014). The TRMM PR data set is used herein to analyze the seasonal and regional variability of several different types of extreme storms.

In the first part of this study, the variability of extreme storms and their rainfall characteristics is investigated over the TSEA region (Figure 1, Section 3). The second part of the study looks specifically at Taiwan and the ingredients supporting extreme storms observed by TRMM in this region (Section 4). Overall, this study uses Taiwan and TSEA as a natural moisture-rich laboratory to study the spectrum of precipitating systems producing heavy rainfall and the ingredients that support such systems, with the goal to improve the prediction of heavy rainfall in the current climate and also understand how climate change may impact future heavy rainfall events.

2. Methodology

This study focuses on understanding the nature of convection in the TSEA region shown in Figure 1. For the purposes of this study, TSEA is divided into nine subregions each with a predominant land or sea type description in Table 1. As the size of the subregions varies, the number of storms in each subregion is a reflection of both the size of the subregions and the climatological frequency of different storm types.

This study identifies the extreme storm events and analyzes the rain echoes from 1998 to 2013 using TRMM PR version 7 rain characteristics (2A23; Awaka et al., 1997) and rainfall rate and profile (2A35; Iguchi, Kozu, et al., 2000; Iguchi, Meneghini, et al., 2000) products. The TRMM PR orbital data are remapped into Cartesian coordinates of 250 m vertical resolution and 5 km horizontal resolution following the methodology from

Table 1
Number of TC-Related and Non TC-Related Storms, Respectively, by Each Extreme Storm Type and Subregion From 1997 to 2013 for Every Month

Storm type	Subregions (land-sea type)						
	N Pacific (Sea)	Southeast China (Land)	Taiwan (Land&Sea)	Philippines Sea (Sea)	Philippines (Land)	South China Sea (Sea)	Indochina (Land)
DCCs	1267: 4268	1542: 7963	136: 337	176: 1534	394: 2583	642: 3530	248: 1595
DWCCs	622: 2451	501: 3198	68: 150	129: 726	102: 638	309: 1222	79: 386
WCCs	899: 6205	144: 1566	80: 205	130: 654	94: 252	327: 1081	81: 164
BSRs	591: 3838	145: 1583	34: 47	45: 128	32: 63	138: 242	26: 41

Houze et al. (2007). The data was geolocated and remapped to accommodate for the beam width and scan width angle geometry into the correct Cartesian grid points in three dimensions. Raining pixels from each storm are categorized into convective or stratiform components from the 2A23 product. Three-dimensional radar reflectivity data are separated into extreme storm types that represent different phases of convective development and organization. We use the definition of four extreme storm types following the "moderate" criteria used in Houze et al. (2015b) to account for the predominantly maritime environment of TSEA. The storm categories are defined as: (a) deep convective cores (DCCs) with ≥30 dBZ echo volumes ≥8 km in altitude; (b) wide convective cores (WCCs) with ≥30 dBZ echo volume ≥800 km^2 in horizontal area; (c) deep and wide convective cores (DWCCs) are storms that satisfy both the DCC and WCC criteria; and (d) broad stratiform regions (BSR) with a contiguous stratiform rain area ≥40,000 km^2 in area.

Although TCs frequently influence the TSEA region, this study only considers extreme storms that do not have a nearby TC influence to simplify the interpretation of the results. We filtered out TC-related storms because the environment and ingredients supporting such storms are likely different from those not affected by TCs due to possible influences on the background wind, moisture, and other rainfall ingredients. As such, the TRMM-identified storms are removed from the database if a TC was within 750 km of the storm location. The TC identification is performed following Brown et al. (2016) which had matched TRMM Microwave Imager swaths with TC best track data. The TC filtering results in a 10%–45% reduction in the number of TRMM-identified storms, depending on the region (Table 1).

For each subregion, the land-sea mask is then applied to the storm core location, considering only storms with center points over only land or sea (Table 1). Taiwan is the only subregion where we consider storm cores that occur both over land and sea, particularly to understand the storm climatology over the region that is relevant for the PRECIP 2022 field campaign.

To focus on the peak rainfall season of the TSEA region, the analysis focus on the monsoonal months of May–September. Only the monthly distribution analysis and the storm number distribution for each subregion are computed over the entire 12 months.

The monthly distribution of each extreme storm type in each subregion is computed over the annual cycle. The number of storms is normalized by the total number of each storm type in each subregion shown in Table 1, because the cumulative number of storms that occur in each subregion is variable and this allows for comparisons across the annual cycle. It is worth noting that the number of BSRs can be significantly lower than other types for some subregions (Table 1). For example, the number of BSRs in Indochina and Taiwan is smaller than the other regions, but their number is still large enough for the monthly distribution analysis.

Rain characteristics are calculated to examine the distribution of the rain intensity (mm/hr) and volumetric rain rate (kg/s) during the extended warm season (May–September). They are computed using the Z-R method for determining surface rainfall from Romatschke and Houze (2011) and Rasmussen and Houze (2016) to correct the bias of the TRMM PR of underestimating the rain intensity over land (Rasmussen et al., 2013) and from storms with higher echo-top heights (Gingrey et al., 2018).

Contoured frequency by altitude diagrams (CFADs) are calculated for storms that fall within the boundaries of the subregions (Figure 1) during the extended warm season. Thus, a storm may be counted toward more than one subregion if they fall across region boundaries. This method is meant to take into consideration the horizontally larger storms (i.e., WCCs and BSRs). To create the CFADs, we sum the full-storm 3D reflectivity of each extreme storm for each subregion by their height and take the histogram of each height level by their reflectivity. The distribution of each level is then normalized by dividing by the maximum number of pixels at that specific height level.

ERA5 reanalysis (Copernicus Climate Change Service (C3S), 2017) is used to calculate the ingredients-based composites of the mesoscale environments supporting extreme storms between 5°–35°N and 97°–150°E during the extended warm season. We select 850 hPa vertical moisture flux and vertically-integrated moisture divergence (VIMD) to represent the intensity factors from Doswell's ingredients-based framework (Equation 1 and the 700–900 hPa low-level shear (LLS) to represent the influence of the Meiyu front (Akiyama, 1973; Sampe & Xie, 2010). To make the daily mean composite maps of these ingredients, we choose the date from the TRMM overpass timestamp of each storm type over Taiwan. The all hourly data from that date from ERA5 is then averaged together to create a daily average composite map of each ingredient during extreme storms over Taiwan.
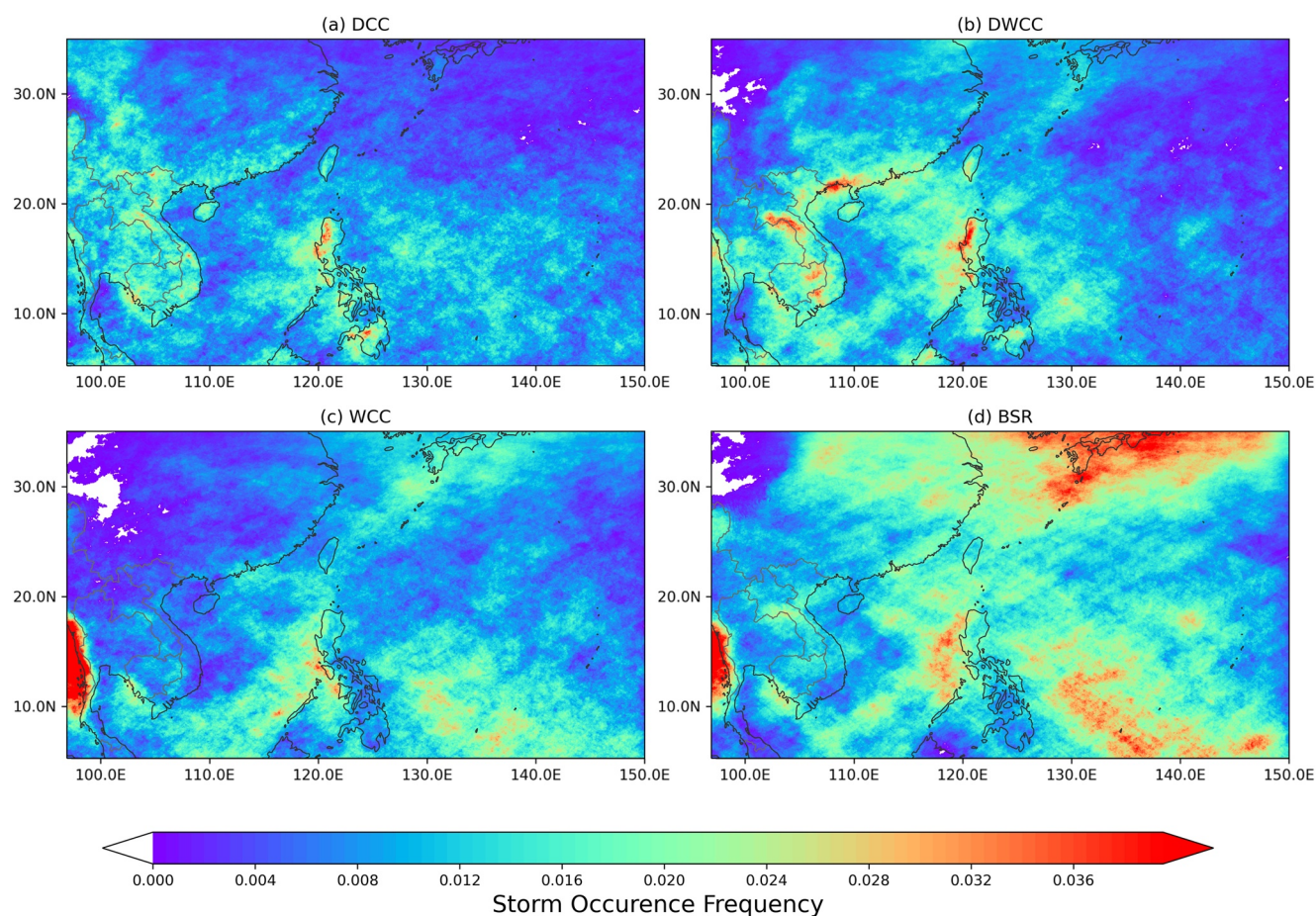
Figure 2. Geographical distribution of the probability of finding (a) deep convective cores, (b) deepwide convective cores, (c) wide convective cores, and (d) broad stratiforms regions over Tropical and Subtropical East Asia during May–September.

This process is repeated for each storm type in each subregion. The time-lag of these ingredients is computed from area-averaged hourly averaged ERA5 data for each subregion from 7 days before to 7 days after the time each echo was observed by TRMM PR.

3. Climatology of Storms Containing Deep Convective Cores, Wide Convective Cores, and Broad Stratiform Regions in Tropical East Asia

3.1. Seasonal and Regional Variabilities of Extreme Radar Echo Structures

To understand the seasonal and regional variability of the spectrum of storms seen by TRMM, we analyzed the monthly distribution of storms with extreme characteristics in each subregion across TSEA. Figure 2 shows the geographical distribution of the probability of finding each extreme echo type (i.e., DCCs, DWCCs, WCCs, and BSRs) from May to September of 1998–2013 using TRMM PR data. The probability is scaled according to the TRMM overpass frequency over each pixel to take into account the differential sampling across latitudes as has been done in previous studies (Houze et al., 2007, 2015b; Romatschke et al., 2010).

Figure 2a shows that DCCs are found throughout the TSEA region, with a notable minimum over the central Pacific Ocean. DCCs tend to cluster along the coastlines and the mountain ranges, suggesting that coastal effects and orographic lifting may influence their development. The distribution of DWCCs (Figure 2b) is similar to DCCs. They cluster even stronger along some coastal and mountain range locations, suggesting that there might be some local effect at play on top of the coastal effects and orographic lifting. It is well established from prior research using the TRMM satellite's PR that the deepest convective storms on Earth occur over land regions (Houze et al., 2015b; Zipser et al., 2006). The primary reason for this preference is the connection to the

significant diurnal heating effects over land that are necessary for the generation of vigorous updrafts with strong buoyancy in general (Yu et al., 2021, and many others).

On the other hand, WCCs and BSRs are found over the oceanic regions (Figures 2c and 2d), suggesting that WCCs share similar environmental ingredients with BSRs despite of WCCs being of convective type. The BSRs are more likely to occur over ocean regions as they often need enhanced moisture on a broader scale, both in time and space perspectives. Thus, oceanic and moist regions around the world tend to have enhanced stratiform activity (e.g., Houze et al., 2015b). Over the North Pacific subregion, BSRs concentrate over the northern border of TSEA. Extreme rainfall in this region is associated with both mid-latitude weather systems influencing the subtropics and the Meiyu front. Over the southern subregions, BSRs concentrate over the South China Sea off the west coast of the Philippines and spread out over the Philippine Sea. These latter high probability locations may be associated with the west Pacific warm pool region, as large areas of stratiform precipitation were documented by the Tropical Ocean Global Atmosphere Coupled Ocean Atmosphere Response Experiment. The region has large regions of stratiform precipitation that developed along the zonal wind shear as influenced by the westerly wind burst from the Kelvin-Rossby wave (e.g., S. S. Chen et al., 1996; Houze et al., 2000). Thus, the probability of BSRs in TSEA is the highest among the extreme echo categories based on their high detection in the TRMM record. However, as Table 1 shows the number of each extreme echo type over each subregion, the absolute number of BSRs are lowest among all types even for the oceanic subregions. Their high probability of detection is a result of their larger horizontal area and tendency to last longer than the other extreme echo types.

Analysis of the normalized monthly occurrence of the extreme storm types in each subregion is shown in Figure 3. The subregions on the *x*-axis are grouped into the northern subregions on the left (i.e., North Pacific, Southeast China, and Taiwan) and the southern subregions on the right, (i.e., Philippine Sea, Philippines, South China Sea, and Indochina). In general, DCCs and DWCCs show similarities in the monthly storm occurrence variability across the subregions (Figures 3a and 3b) with the exception of North Pacific and Taiwan. In contrast, the monthly distribution of WCCs differs from DWCCs (WCCs with deep components), particularly those in northern subregions (Figure 3c). The distribution of BSRs is different from the convective categories, suggesting that the environment supporting BSRs varies from those supporting convective categories. The northern and the southern subregions also show similarities in monthly storm occurrence for DCCs and DWCCs storm types.

In the northern subregions, DCCs and DWCCs show a higher probability of occurrence in the summer. Southeast China DCC and DWCC storms peak in July and have a similar monthly frequency pattern, with a slightly earlier occurrence of DWCCs from April compared to DCCs (Figures 3a and 3b), implying that the subregion has sufficient ingredients for both DCCs and DWCCs at the same time. DCCs in the Taiwan and North Pacific regions have a similar shape in the seasonal distribution, possibly suggesting similar seasonal shift of environment, such as large scale upward motion, during the peak of the East Asian summer monsoon season (Ding & Chan, 2005; Trenberth et al., 2000). While DCCs in Taiwan peak in July, those in the North Pacific region peak in August (Figure 3a). Their DWCC counterparts peak a month earlier than their DCCs, in June for Taiwan and July for North Pacific (Figure 3b), suggesting that there is some difference in the environment that support the congregation of convective cores from DCCs into the larger DWCCs in the earlier months. The Taiwan and North Pacific DWCCs occurrence frequency patterns also differ more from each other. While Taiwan shows a May–September occurrence, the North Pacific frequency skews toward the second half of the year.

The southern subregions have a broader spread in occurrence with double peaks in the spring and fall seasons for DCCs and DWCCs (Figures 3a and 3b), a characteristics of precipitation observed in the region (Lau & Yang, 1997). To illustrate, Indochina and the Philippines are both "land-only" regions and have a similar distribution. The distribution of DCCs in these regions each has a peak in late spring (i.e., May) and a lower peak in September. DWCCs in Indochina and the Philippines also have a similar distribution compared to DCCs (Figures 3a and 3b), but with an even higher probability of occurrence in spring and summer, peaking from May to July with higher relative frequency in September, highlighting that the environment during the spring and summer season is favorable for both DCCs and even more for DWCCs in Indochina and the Philippines.

On the other hand, the Philippine sea DCCs occur primarily in fall and winter, peaking in September and October, but also have a secondary peak in May earlier in the year. Philippine sea DWCCs also show a similar frequency pattern, peaking higher in May and September. The South China Sea DCCs shows an almost equal probability for spring-to-summer and fall-to-winter occurrences, with a DCC maxima in May and June before increasing again in September. The South China Sea DWCC frequencies do not increase in spring or early fall like the
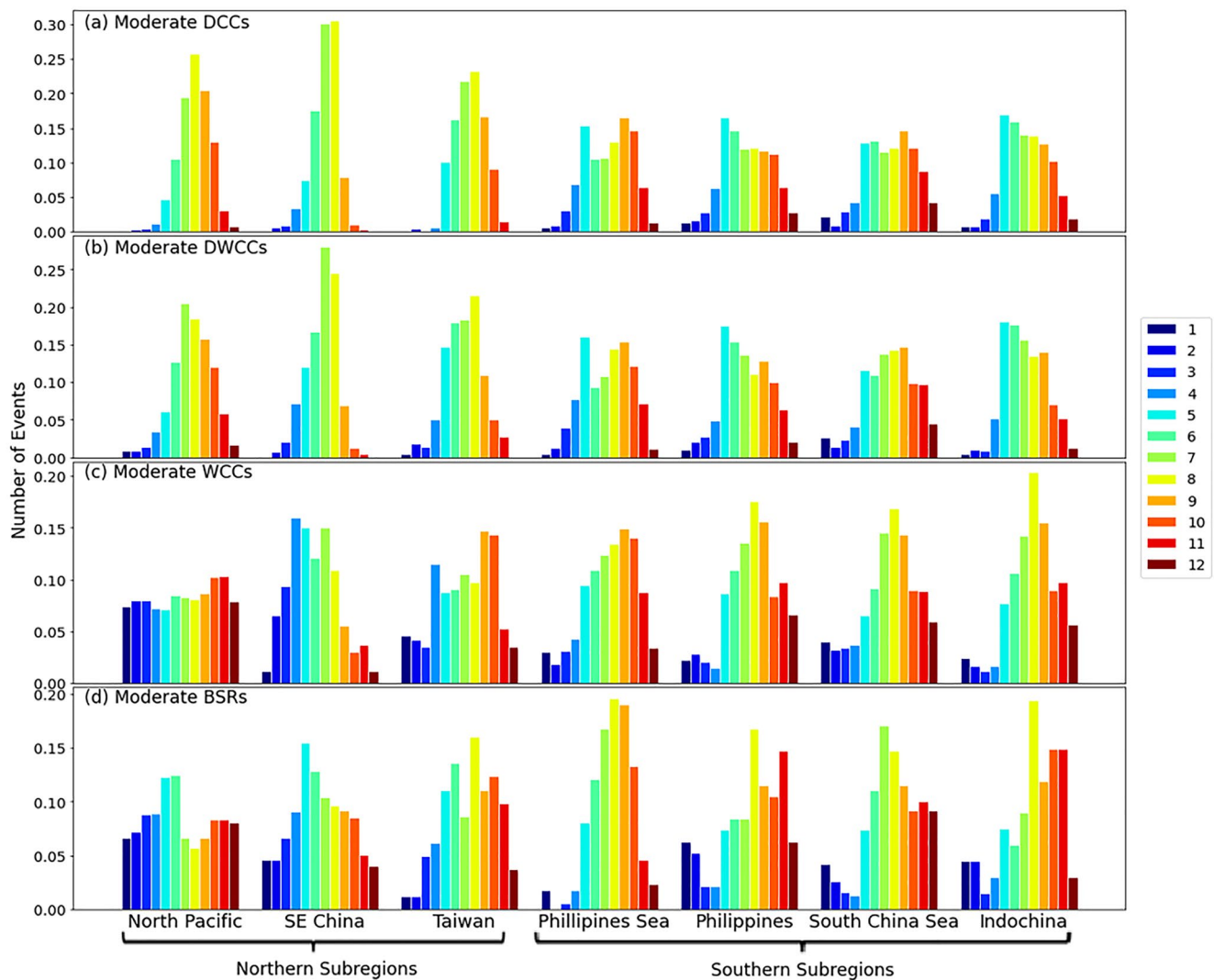
Figure 3. Normalized monthly occurrence distribution of (a) deep convective cores, (b) deepwide convective cores, (c) wide convective cores, and (d) broad stratiforms regions in each subregion as observed by TRMM PR from 1998 to 2013. Colors denote each month of the year.

other southern subregions, with a more uniform distribution while still having a similar seasonal distribution for summer-to-winter like South China Sea DCCs. The difference between the land and sea subregions suggests that there is the difference between their environment that may play a role in the southern subregions.

Even though DWCCs and WCCs share the same echo area criteria, WCC distributions differ from DWCC, especially in the northern subregions (Figure 3c). The biggest contrast is in North Pacific, where WCCs occurs more uniformly across the year compared to DWCCs. On the other hand, Southeast China's WCC distributions peak earlier in April–May in association with the regional spring rain (LinHo et al., 2008), while DWCCs maximize later in July. Taiwan WCCs show bimodal occurrence distributions, peaking in April also in association with the spring rain (Hung et al., 2004) with a secondary maximum occurring in October possibly due to early Early winter cold front which occur mostly to the Northeast of Taiwan (C.-S. Chen & Chen, 2003; Henny et al., 2021). This frontal system should provide the shear for the storm to develop structure into larger storms. This Taiwan WCC distribution contrasts its DWCC distributions peaking in June.

In the southern subregions, WCCs show less of a bimodal distribution than DCCs and DWCCs. Southern WCC distributions essentially peak in between the two modes of DCCs and DCCs over the summer months into September while maintaining the majority of occurrence between May and November. The Philippine Sea WCCs show broad occurrences from May to November, significantly higher than the other months. The Philippines and

South China Sea WCCs have sharper peaks from July to September and a lower peak in November. Indochina similarly shows a peak in July and August. These southern subregions' WCC distributions are related to the maritime-continent monsoon (Chang et al., 2005).

The distribution of BSRs is distinct from the convective categories. In the northern subregions, BSR distributions all peak in May–June. Southeast China's DCC and DWCC distributions tend to maximize earlier in the year, while the WCC and BSR distributions tend to maximize later in the year. One difference between WCCs and BSRs in Southeast China is that WCCs peak from April to July and are infrequent in the winter months, while the BSRs peak in May. However, the BSR frequency in the North Pacific is not as uniformly spread, but rather peaks in May and June and decreases quickly to the August minimum, which is when TC-related events were removed the most (Table 1). Taiwan BSRs also peak a month after WCCs in May and June and drop sharply in August and September, before picking up again over October and November (Figure 3d).

The variability of the maximum month of occurrence across the northern subregions for BSRs reflects the northward movement of the Meiyu front (Ding, 1992; Ding & Chan, 2005). The front establishes over Taiwan and Okinawa, Japan, in mid-May from the confluence of mid-latitude eddies and southerly moist air, marking the onset of the East Asian Monsoon, and progress northward to the Yangtze River Valley in China and mainland Japan (out of our region of interest) from mid-June to mid-July (Akiyama, 1973; Ding & Chan, 2005; Sampe & Xie, 2010). The Meiyu front is a convective rainband that occurs along a stationary front with a steep gradient of specific humidity, equivalent potential temperature, and low-level wind shear (Akiyama, 1973; Ninomiya & Shibagaki, 2007). We will use low-level wind shear as a proxy to mark the location of the Meiyu front relative to the extreme storms later in this study.

In the southern subregions, BSRs peak in July for sea-only subregions and over the end of the year for the land-only subregions. The sea-only subregions also have similar occurrence distribution shape to their WCCs counterpart. The Philippine Sea BSRs peak in July but also in September, with a narrower distribution compared to WCCs. The South China Sea BSRs also hold a similar distribution shape to WCCs, but with smaller variability as well, peaking largely in July with a smaller peak in December. On the other hand, the land-only BSRs do not have similar occurrence distribution shape to their WCCs counterpart. Philippines and Indochina BSR occurrence distribution is relatively flat with a peak later in the year, in November and December respectively.

Overall, DCCs and DWCCs are shown to have a similar monthly distribution within northern regions with one peak, and southern subregions with having two peaks. WCC distributions differ from DWCC, especially in the norther subregions, even though they share the same echo area criteria. The BSR distribution differs from the convective categories, suggesting that the environment supporting BSRs varies from others. In the northern subregions, BSRs are influenced by the East Asian summer monsoon and the accompanying Meiyu front.

3.2. Variability of Rainfall Characteristics for Extreme Storm Categories

A key characteristic of the extreme storm climatology is rainfall intensity, from which important features of the extreme storm variability and hydrometeorological impact across the TSEA region can be assessed. To focus on the heavy rainfall season, the analysis will focus on the monsoonal months of May–September from this point onward. Figure 4 shows that storms containing extreme convective cores (i.e., DCCs, DWCCs, and WCCs) generally produce higher rain rates than storms containing large stratiform regions (i.e., BSRs). The convective events produce higher rain rates overall compared to stratiform rainfall, which is consistent with prior research on this topic (Ulbrich & Atlas, 2002).

Among the convective core storms, DCCs and DWCCs produce a higher mean rain rate of about 5 mm/hr compared to 4 mm/hr associated with the WCCs (Table 2). Thus, deep convective storms with significant reflectivity values at higher altitudes compared to WCCs tend to produce higher rain rates. One interesting result from another study using TRMM radar observations is that the heaviest rainfall-producing storms are not necessarily the tallest storms due to the importance of warm-rain processes (Hamada et al., 2014). Although their study looked at different regions of the world, it is important to note the similarities and differences between our results. One important point is that the TRMM 2A25 rain rate product as used in Hamada et al. (2014) tends to underestimate rain rate in highly convective storms over land due to attenuation in TRMM Ku-band and non-uniform beam filling (Gingrey et al., 2018; Iguchi et al., 2009; Rasmussen et al., 2013). In response to this underestimation, the TRMM rain rate is computed with a Z-R relationship to avoid the low rain bias as was previously done in
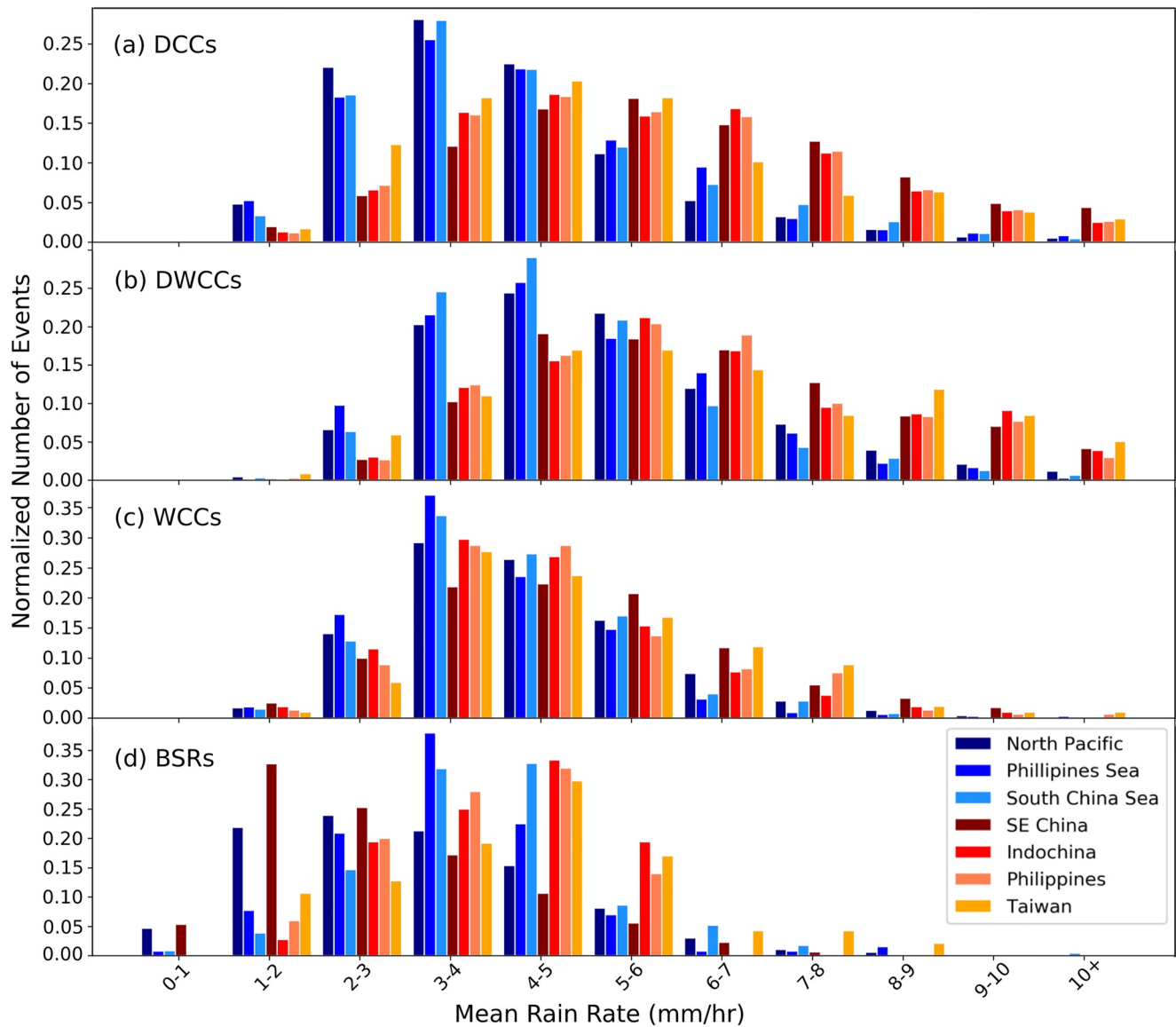
Figure 4. Normalized frequency of mean rain rate of (a) deep convective cores, (b) deepwide convective cores, (c) wide convective cores, and (d) broad stratiforms regions in each subregion during May–September. The blue bars represent the sea-only subregions. The orange bars represent the land-only subregions, and the yellow bar represents Taiwan.

Table 2
Mean and Standard Deviation of Full Storm Mean Rain Rate and Volumetric Rain for Each Storm Type During May–September

Statistics of rain characteristics	DCCs			DWCCs			WCCs			BSRs		
	Land	Sea	All	Land	Sea	All	Land	Sea	All	Land	Sea	All
Mean of mean rain rate (m/s)	5.31	4.49	5.00	6.36	5.00	5.69	4.99	4.17	4.37	3.05	3.43	3.22
Standard deviation of mean rain rate (m/s)	3.27	1.85	2.86	2.55	1.79	2.31	2.25	1.33	1.64	1.51	1.42	1.45
Mean of Volumetric rain (kg/s)	5.85	12.80	8.48	16.89	5.00	5.69	19.56	24.27	23.19	71.61	84.66	80.99
Standard deviation of Volumetric rain (kg/s)	14.65	27.84	20.94	26.27	39.28	2.31	31.59	37.39	36.20	48.22	51.67	51.06

Note. BSRs, broad stratiforms regions; DCCs, deep convective cores; DWCCs, deepwide convective cores; WCCs, wide convective cores.

Rasmussen et al. (2013) and suggested in Gingrey et al. (2018). Thus, at least for the moisture-rich environment of TSEA, the heavier rainfall producing storms are associated with taller and more intense convective storms. Moreover, DWCCs that met both the height and area requirement produced a slightly higher mean rain rate than DCCs, as shown in Figure 4b. The larger storm area, mesoscale processes, and convective organization associated with DWCCs might help to increase rainfall through a reduction in dry air entrainment and other mesoscale dynamics that enhance vertical motion within organized convection (e.g., Rotunno et al., 1988). However, the difference between the DCCs and DWCCs mean rain rate distribution shape is sensitive to the selected interval. When increasing the interval to 2 mm/hr, the rain rate difference between the storm modes disappears.

The rain rate distribution in each subregion also highlights the differences between storms over land and sea. The warm colors indicate land-only regions and the cool colors indicate ocean-only regions, with the exception of Taiwan (yellow bars) that include both land and ocean regions. Rain rates over land subregions and Taiwan are higher than those over the sea subregions for almost all storm types. The difference is more obvious for the deeper storms than the wider storms. For DCCs (Figure 4a), the difference between the mean rain rates for ocean-only compared to land-only regions is evident across all subregions. This difference indicates that despite the variation in topography, land-surface type, and location across TSEA, all land-only regions have heavier convective rainfall compared to those over oceanic regions. The difference is less pronounced for DWCCs where the sea-only rain rates increase to 4–5 mm/hr while the land-only rain rates stay the same (Figure 4b). Interestingly, the WCC rain rates for land- and sea-only show a much closer distribution, with the land-only rates being slightly higher overall (Figure 4c). This result suggests that storms with deep convection are more vigorous over land with higher rain rates, but storms with wide convective echoes have a similar rain rate distribution over both land and sea.

In contrast to the clear distribution in convective rain rates shown in Figures 4a–4c, the rain rate distribution between land- and sea-only regions is more complex. As shown in Figure 4d, Southeast China is an outlier subregion with low mean rain rates of 1–2 mm/hr, while the other land-only subregions peak at 4–5 mm/hr. The sea-only subregions average around 3–4 mm/hr, which is lower than the land-only regions, except for Indochina. Higher rain rates over land can be explained by a more pronounced diurnal cycle than over the sea surface due to stronger daytime heating and nocturnal cooling over land regions (Yu et al., 2021). Orographic lifting could also help enhance the air motions and diurnal cycle.

Another important rainfall metric beyond the mean intensity of the rain is the total rain volume produced by each extreme storm type shown in Figure 5. Volumetric rain can show the total rain accumulation the entire system can produce and more accurately represents the overall influence of the convective storm size and intensity relative to a mean rain rate estimate. In addition, volumetric rain is connected with the latent heat produced by the storm and is therefore important to examine in combination with the rain rate.

Despite producing the highest mean rain rates, DCCs produce the smallest amount of volumetric rain. DCC volumetric rain is smaller than DWCCs and WCCs by 10 times and BSRs by 20 times. This result is consistent with results from Rasmussen and Houze (2016) who showed that DCCs have the lowest percentage of rain contribution to the total rainfall compared to DWCCs, WCCs, and BSRs in subtropical South America. DCCs often represent the early phase of the convective lifecycle with vigorous, relatively short-lived and sometimes isolated convective cells that produce heavy rainfall locally, but do not tend to last for long periods of time (Houze et al., 2007, 2015b). There is also no obvious volumetric rain distribution difference between the storms over land and sea (Figure 5a), contrasting with the distinct distributions of the mean rain rate distributions in Figure 4a. DWCCs also show the land-only regions skewed toward lower volumetric rain than the sea-only regions (Figure 5b). Given that the DWCC rain rates are also higher over the land than over the sea (Figure 4b), the DWCCs over land are generally smaller in size than those over the seas. In fact, DCCs and DWCCs over the sea have about double the mean horizontal area than those over land (Table 3). Overall, BSRs produced the most volumetric rain (Figure 5d), up to 20 times larger than DCCs due to the large horizontal area (Table 3).

Despite producing the lowest mean rain rates (Figure 4d), BSRs can produce the largest volume of rain. On the other hand, DCCs produced the least volumetric rain despite having the highest rain rates (Figure 5a), due in large part because the area is significantly smaller than DWCCs and WCCs (Table 3). Given that storm size is a factor in the rainfall duration of the ingredients-based approach (Equation 1; Doswell et al., 1996), understanding how both mean and volumetric rain rates vary across the storm modes provides important information on the hydro-meteorological impact in the TSEA region.
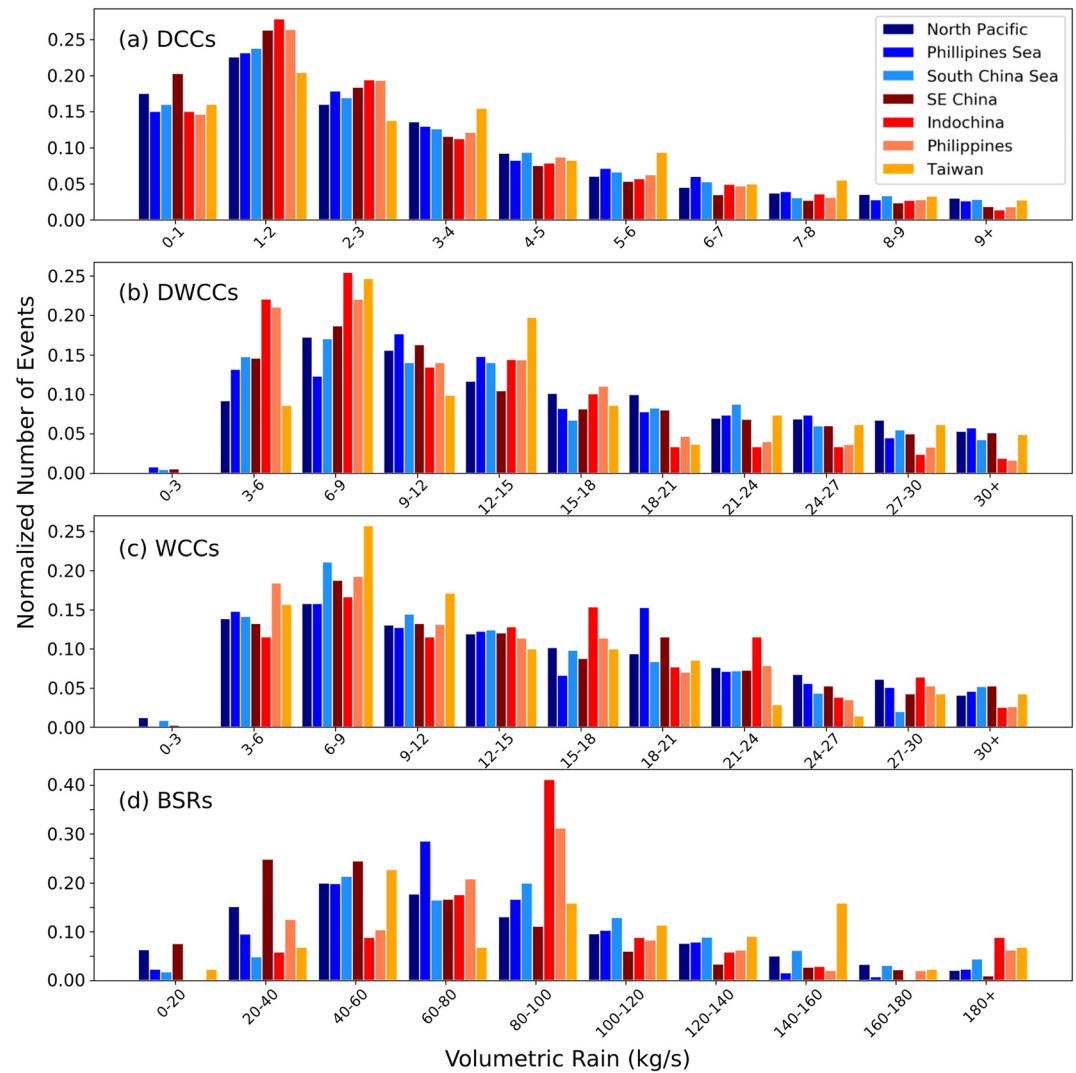
Figure 5. Same as Figure 4, but for volumetric rain.

3.3. Contoured Frequency by Altitude Analysis

Contoured Frequency by Altitude Diagrams (CFADs; Yuter & Houze, 1995) of the storm reflectivities from TRMM PR observations provide insights into the horizontal and vertical characteristics of the storms producing the rainfall described in Section 3.2. We normalized the frequency by the maximum frequency at a given altitude as is typical for CFAD analyses.

Figure 6 shows the normalized frequency of the reflectivity at a given height from all reflectivity observations captured by TRMM PR observations from May to September 1998–2013 in the TSEA region. The horizontal line

Table 3
Mean and Standard Deviation of Full Storm Area for Each Storm Type During May–September

Statistics of storm area	DCCs		DWCCs		WCCs		BSRs	
	Land	Sea	Land	Sea	Land	Sea	Land	Sea
Mean (km^2)	12,847	31,394	25,555	45,667	35,650	50,641	91,737	96,753
Standard deviation (km^2)	20,522	38,043	28,590	41,781	39,373	45,829	41,154	42,546

Note. BSRs, broad stratiforms regions; DCCs, deep convective cores; DWCCs, deepwide convective cores; WCCs, wide convective cores.
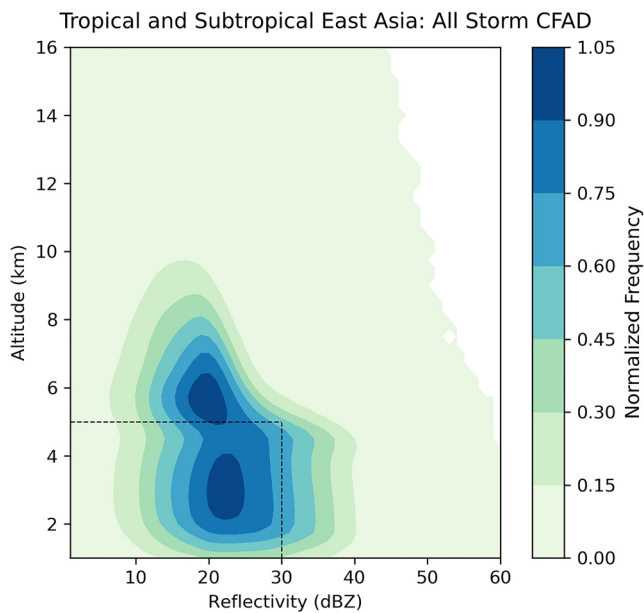
Figure 6. Contoured frequency by altitude diagram of all raining objects over Tropical and Subtropical East Asia during May–September.

at 5 km is marked as a reference for the approximate melting level, where the reflectivity is shifted to the right just below 5 km in Figure 6 due to the melting ice particle's higher reflectivity or bright band. The vertical reference line at 30 dBZ marks where the low-level reflectivity frequently occurs from 20 to 30 dBZ, corresponding to the rain rate at the surface of up to 1–3 mm/hr. This estimated general rain rate is similar to that found during the Indian summer monsoon season in the Himalayan region of 1–2 mm/hr (Houze et al., 2007). That region is located in the tropics and subtropics and is affected by the summer monsoon similar to the TSEA region, but is located outside of the West Pacific warm pool.

To highlight the differences in the storm structures, the CFAD anomalies of each storm type and subregion are computed by subtracting the full TSEA CFAD (Figure 6) from each CFAD for DCCs, DWCCs, WCCs, and BSRs (Figures 7–10). The resulting CFAD anomalies of storms containing extreme convective cores (e.g., DCCs, DWCCs, and WCCs; Figures 7–9) show generally higher frequencies (positive anomalies) of reflectivity greater than 30 dBZ at low-levels and lower frequencies (negative anomalies) of reflectivity less than 30 dBZ from low-levels to slightly above the melting level. The higher reflectivity at low-levels for convective cores (Figures 7–9) compared to all of the raining data (Figure 6) is consistent with higher rain rate distributions compared to stratiform precipitation (Figure 4). The positive anomaly above the melting level demonstrates the strong convection characteristics by region in both height and vigor.

Among the three extreme convective core categories, DCCs and DWCCs share similar CFAD anomaly profiles (Figures 7 and 8), with strong reflectivity from the base to the cloud top, with a notable increase in reflectivity frequencies above the melting layer that reflects the convective core top height requirement. The land-only subregions (Southeast China, Philippines, and Indochina; Figures 7 and 8c, 8e, 8g) show that low-level reflectivity is also higher than the sea-only subregions by 5–10 dBZ, in agreement with to the rain rate distributions in Figures 4a and 4b that the land-only rain rate mode is higher than the sea-only one. The land-only subregions also show a connected area of increased frequencies of reflectivity both above and below the bright band for both DCCs and DWCCs, indicating stronger convection overall. The Taiwan CFAD anomalies show the hybrid pattern of the land- and sea-only subregions. Even though Taiwan DCCs have a connected region of higher frequencies above and below the melting level like the land-only DCCs, Taiwan DWCCs have a stronger bright band like the sea-only DWCCs indicating the presence of larger stratiform precipitation regions over Taiwan associated with DWCCs compared to other regions.

Although WCCs have a higher frequency of high reflectivity values below the melting level (Figure 9) compared to the average TSEA rain CFAD (Figure 6), the magnitude is still lower than those associated with DCCs and DWCCs (Figures 7 and 8). The lower reflectivities also correspond with the lower rain rate distributions in Figure 4. Another distinct feature of WCCs from DCCs and DWCCs is that there is no obvious difference between the storms over land and ocean. However, WCCs in the northern subregions (West Pacific, Southeast China, and Taiwan; Figures 9b, 9d, and 9f) show a greater frequency of high reflectivity values at lower levels compared to those in the southern subregions (Philippines Sea, Philippines, South China Sea, and Indochina; Figures 9c, 9d, and 9g). Interestingly, the West Pacific WCCs do not show a strong bright band signal.

The CFAD patterns for BSRs in TSEA (Figure 10) show similarities to WCCs (Figure 9). Although the CFADs do not show obvious differences in storms over land and sea, there is a difference in the northern and southern regions of TSEA. The most northern subregions, West Pacific and Southeast China, show BSRs with weak reflectivities overall. The four southern subregions show stronger bright bands, similar to their counterparts in WCC CFAD structures. Taiwan, in the middle of the two regions, shows a mix of both features with weak negative anomalies for low reflectivity values under the melting level with only a slight bright band enhancement. Robust stratiform regions with stronger brightband, such as those in the West Pacific warm pool, are usually connected
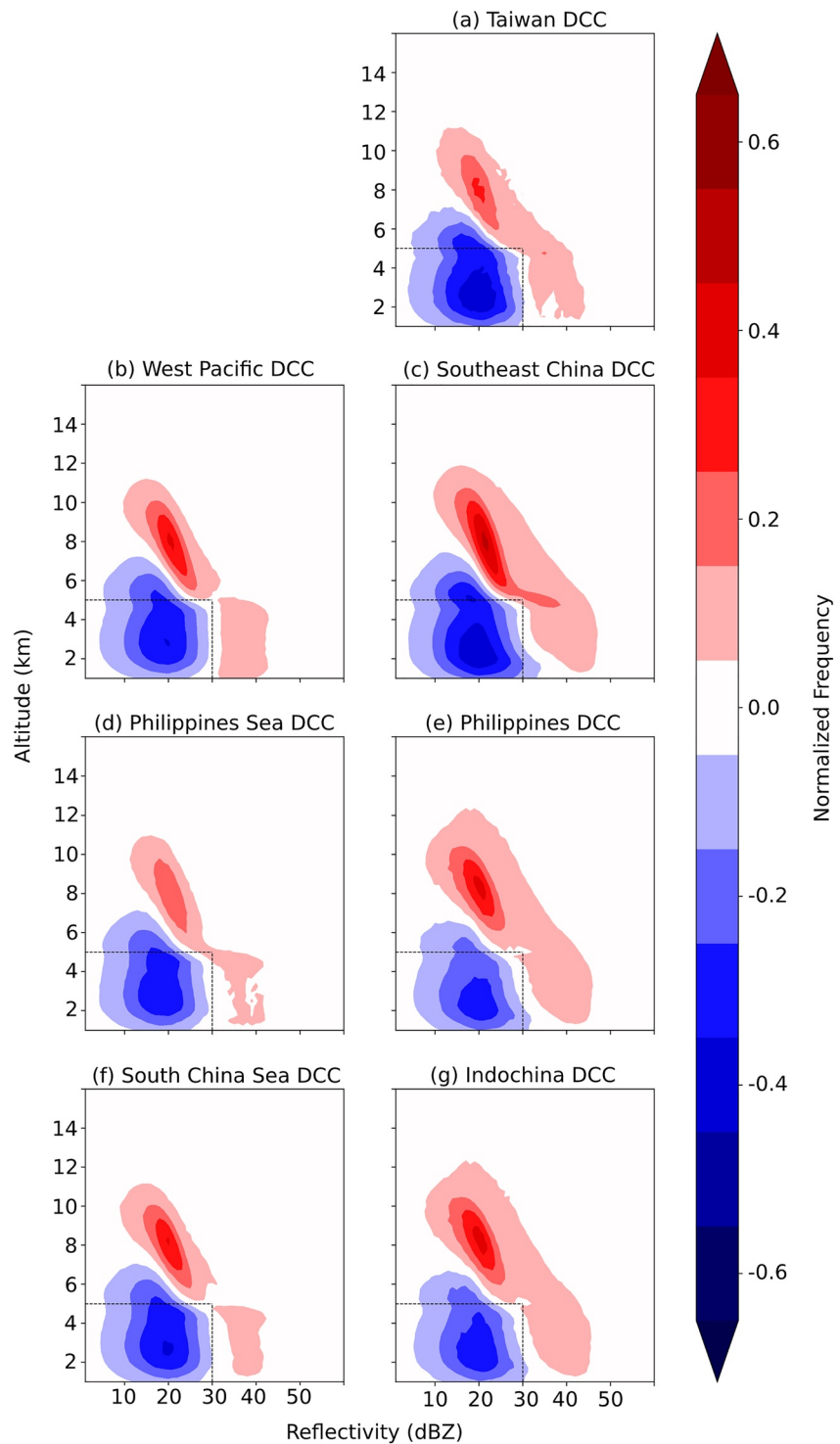
Figure 7. Contoured Frequency by Altitude Diagrams of deep convective cores for (a) Taiwan, (b) North Pacific, (c) Southeast China, (d) Philippines Sea, (e) Philippines, (f) South China Sea, and (g) Indochina during May–September. The left column represents sea-only subregions (b, d, f). The right column represents land-only subregions (c, e, g) and Taiwan.

with deep and intense convective echoes (Houze et al., 2015b). From the number of storms shown in Table 1, ratio of the convective cores to BSRs in the southern subregions are higher than in the norther subregions. It is possible that a good number of these convective cores were embedded in the BSRs, and support the formation of these brightband and stronger reflectivity overall of the BSRs.
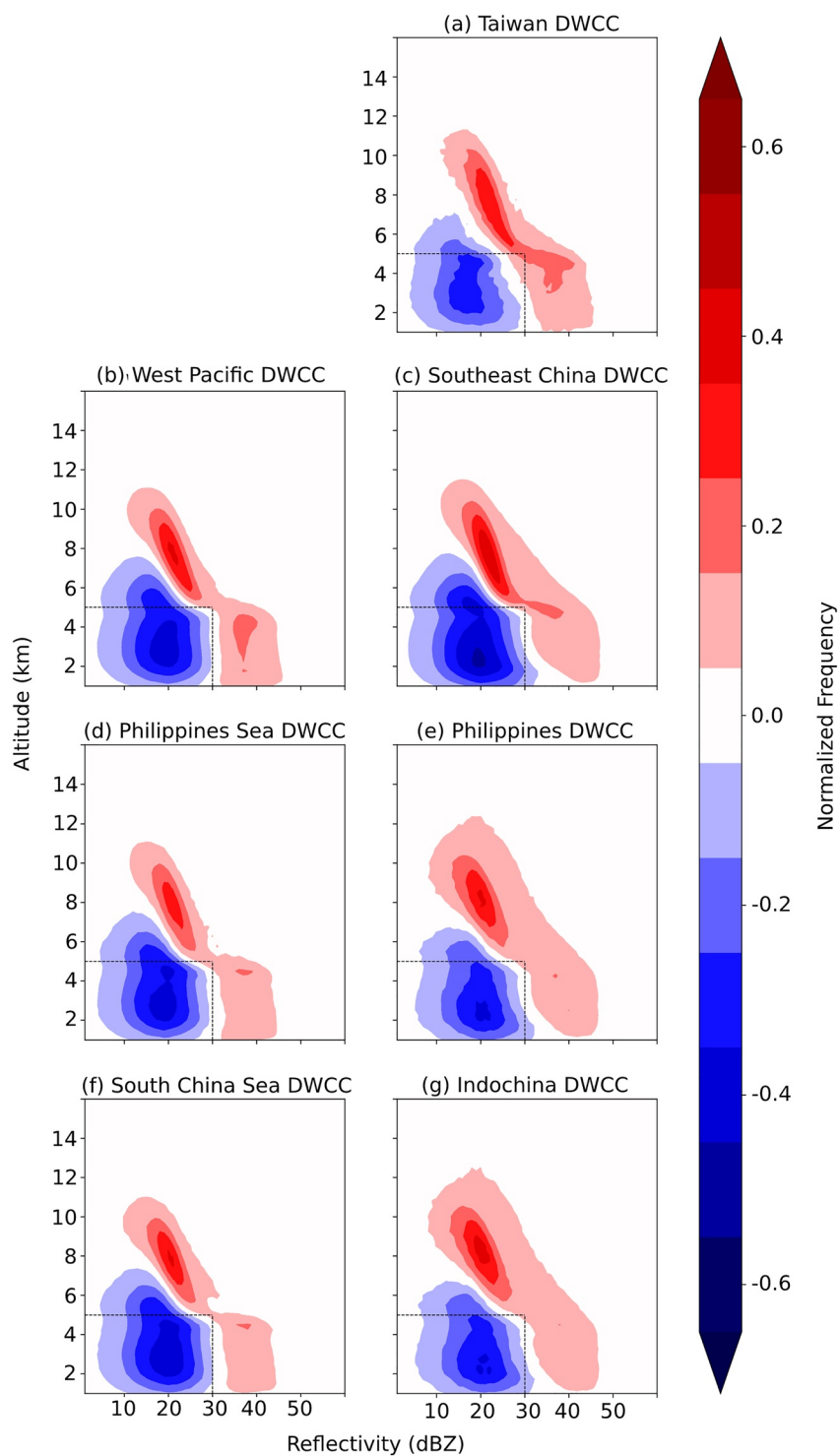
Figure 8. Same as Figure 7, but for deepwide convective cores.

From the storm structure analysis in these subregions, Taiwan shows an interesting mix of factors influencing its extreme storms. The Taiwan subregion also combines the moisture-rich environment over the sea and the orographic lifting from the Central Mountain Range, mixing properties of both land and sea regions. Its location in the northern half of TSEA allows for the clear rain signal of the well-studied East Asian summer monsoon rain signal associated with the Meiyu front. Thus, the Taiwan subregion will be a focus for the remainder of the paper.
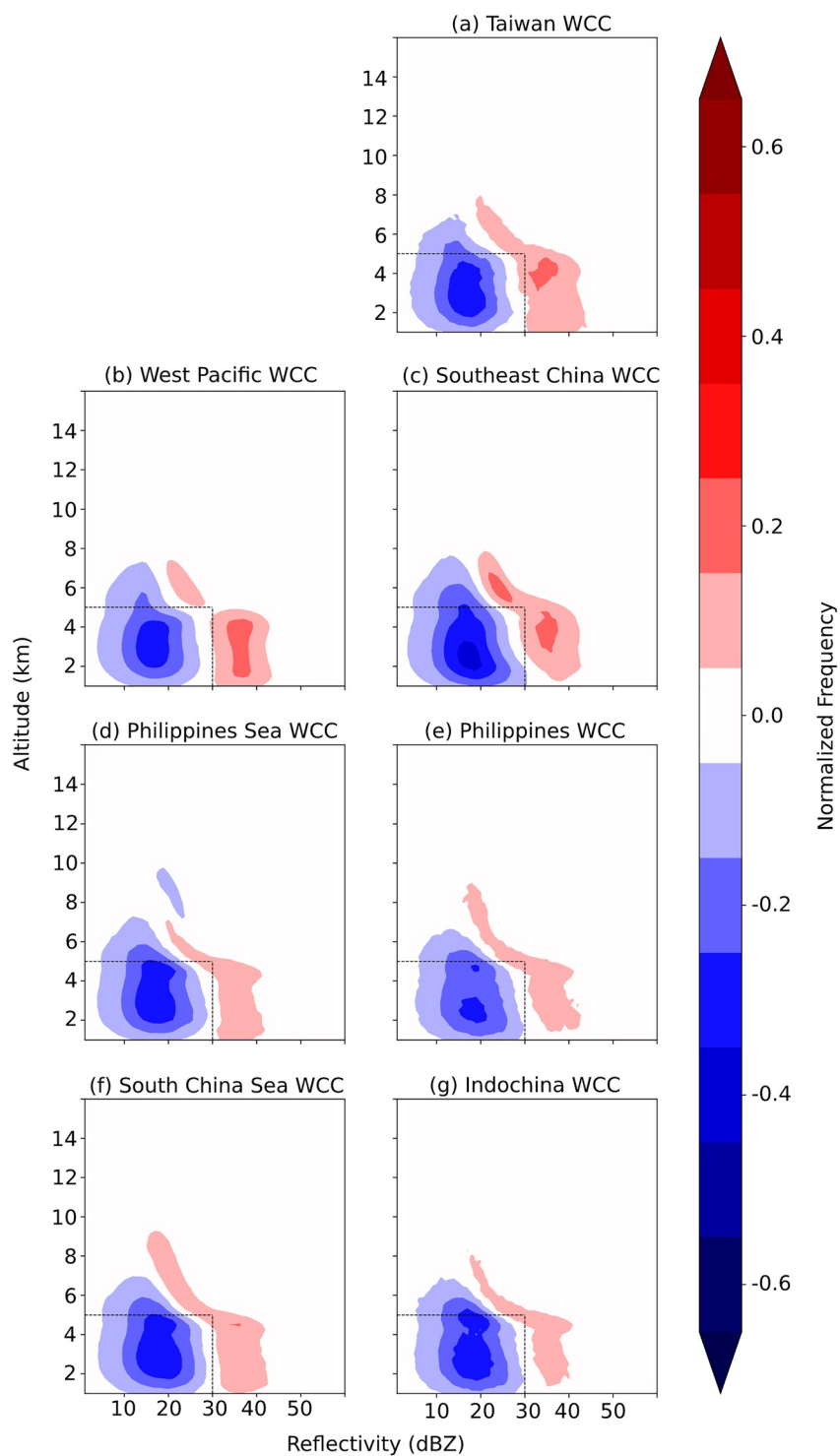
Figure 9. Same as Figure 7, but for wide convective cores.

4. Ingredients for Heavy Rainfall Over Taiwan

The primary reason that Taiwan was selected is to provide context for the large international field campaign called PRECIP (Prediction of Rainfall Extremes Campaign in the Pacific) that took place in summer 2022 in the vicinity of Taiwan.
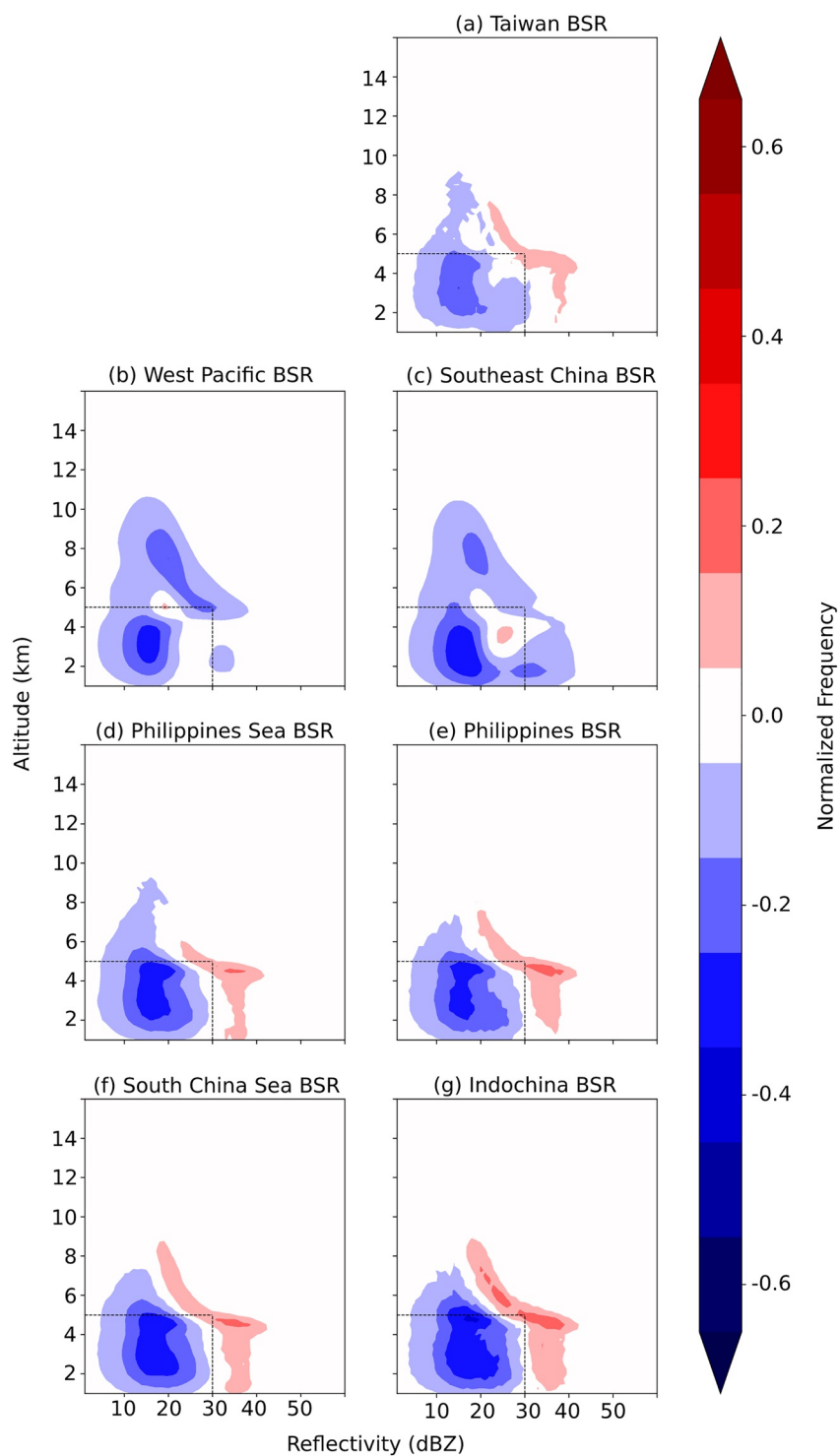
Figure 10. Same as Figure 7, but for broad stratiforms regions.

In addition to being the focal point for a recent field campaign, Taiwan is a unique subregion in TSEA. The rain intensity in that region is skewed toward higher rain rates and volumetric rain (Figures 4 and 5), even when compared with the other land-only subregions in TSEA. This characteristic implies that the unique topography of Taiwan and enhanced diurnal heating associated with thermal contrasts between the mountains and surrounding land amplifies the "land" characteristics seen across all extreme storm types.

However, in terms of meso- and larger scale environment, it is a mix of both land and sea environments and is most similar to the other northern subregions, when they are influenced by the Meiyu front. Taiwan's DCCs and DWCCs exhibit CFAD structures that are a mix of both land- and sea-only subregions. The monthly occurrence frequencies of Taiwan WCCs and BSRs are consistent with the timing of the Meiyu Front as the dominant synoptic to mesoscale phenomena during the late spring and early summer. However, the Taiwan BSR CFAD structure shows a mix of northern and southern features with a slight brightband enhancement that is not as strong as the southern subregions, but is more prominent than in the northern subregions.

4.1. Daily Composite Maps

To investigate the ingredients supporting these heavy rainfall producing systems, a time-lagged perspective of the ingredients (Equation 1) is analyzed for each extreme echo type using composite analysis techniques. Vertical moisture flux and VIMD are used to represent the moisture and vertical motion perspective within the ingredient-based framework (Equation 1; Doswell et al., 1996). 700–900 hPa LLS is selected as a parameter to identify the general Meiyu Front location (Akiyama, 1973).

Summary composites are presented based on the occurrences of each storm type in the Taiwan subregion for some of the ingredients important to producing heavy rainfall to identify the large-scale forcing and features supporting the occurrence of local extreme events.

Figure 11 shows the composite map of daily mean vertical moisture flux and the horizontal wind at 850 hPa on the day when TRMM-identified storm types occurred in the Taiwan subregion. The vertical moisture flux (ωq flux) is the vertical forcing for rainfall intensity in the Doswell et al. (1996) framework (Equation 1). We expect to see higher ωq flux in the environments of storms with higher rain rates. The composite map shows overall weak negative flux (upward direction in the pressure coordinate) over the TSEA region (Figure 11), as is expected of this high-moisture tropical region. Mid-level southwesterly wind from the South China Sea is seen near Taiwan for all extreme echo types. For the DCC and DWCC composites, southerly winds over the South China Sea are directed toward the Southeast China region (Figures 11a and 11b), where the ωq flux is enhanced over this area.

The ωq flux for days when DCCs were observed in the Taiwan subregion shows negative peaks of -0.002 Pa/s over Taiwan, which is not much stronger in magnitude than the moisture flux of the surrounding Pacific (Figure 11a). Thus, DCCs over Taiwan may not need meso- or larger scale ωq flux ingredients and are likely more influenced by strong diurnal heating of the Central Mountain Range and orographic effects (Kerns et al., 2010; Lin et al., 2011). However, it is likely that the ERA5 resolution is not fine enough to represent the strong local-scale forcing expected in strong, convective DCCs to draw any conclusions about the local scale vertical forcing.

The 850 hPa winds for days when DWCCs were observed in the Taiwan subregion is stronger than for DCCs over the Pacific and the South China Sea (Figure 11b). The downward and upward ωq flux over Taiwan are larger in magnitude. The upward ωq flux over the southwest region of Taiwan also covers a broader area. The upward ωq flux over Taiwan covers an even broader area in the composite for the WCCs (Figure 11c). The region of negative ωq flux extends from the northwest to southwest regions of Taiwan and connects with the negative flux area over the Southeast China region.

The storm type with the most prominent pattern of strong negative ωq fluxes is BSRs (Figure 11d). The downward ωq flux peaks over the southwest coast of Taiwan with a zonal orientation from the Southeast China to the Pacific Ocean east of Taiwan. Coincidentally, the southwesterly wind from the South China Sea that flows over Taiwan is stronger relative to the other storm types, supporting the large upward ωq flux in the Taiwan subregion. Thus, broader and longer-lived storms over the Taiwan subregion require a larger-scale ωq flux. A large amount of moisture available for WCCs and BSRs is possibly supported by the mid-level wind transporting moisture from the South China Sea to the Taiwan subregion, and possibly by the Meiyu front that may explain the upward ωq flux region from the north of South China Sea toward West Pacific Ocean.

To further explore the horizontal transport of moisture, Figure 12 shows composites of VIMD for days when the extreme echoes were observed in the Taiwan subregion. The overall TSEA region shows moisture convergence consistent with Figure 11. Thus, the area does not only produce its moisture locally as expected from a tropical oceanic environment, but also supplies the moisture to the nearby regions. Notable positive VIMD regions are
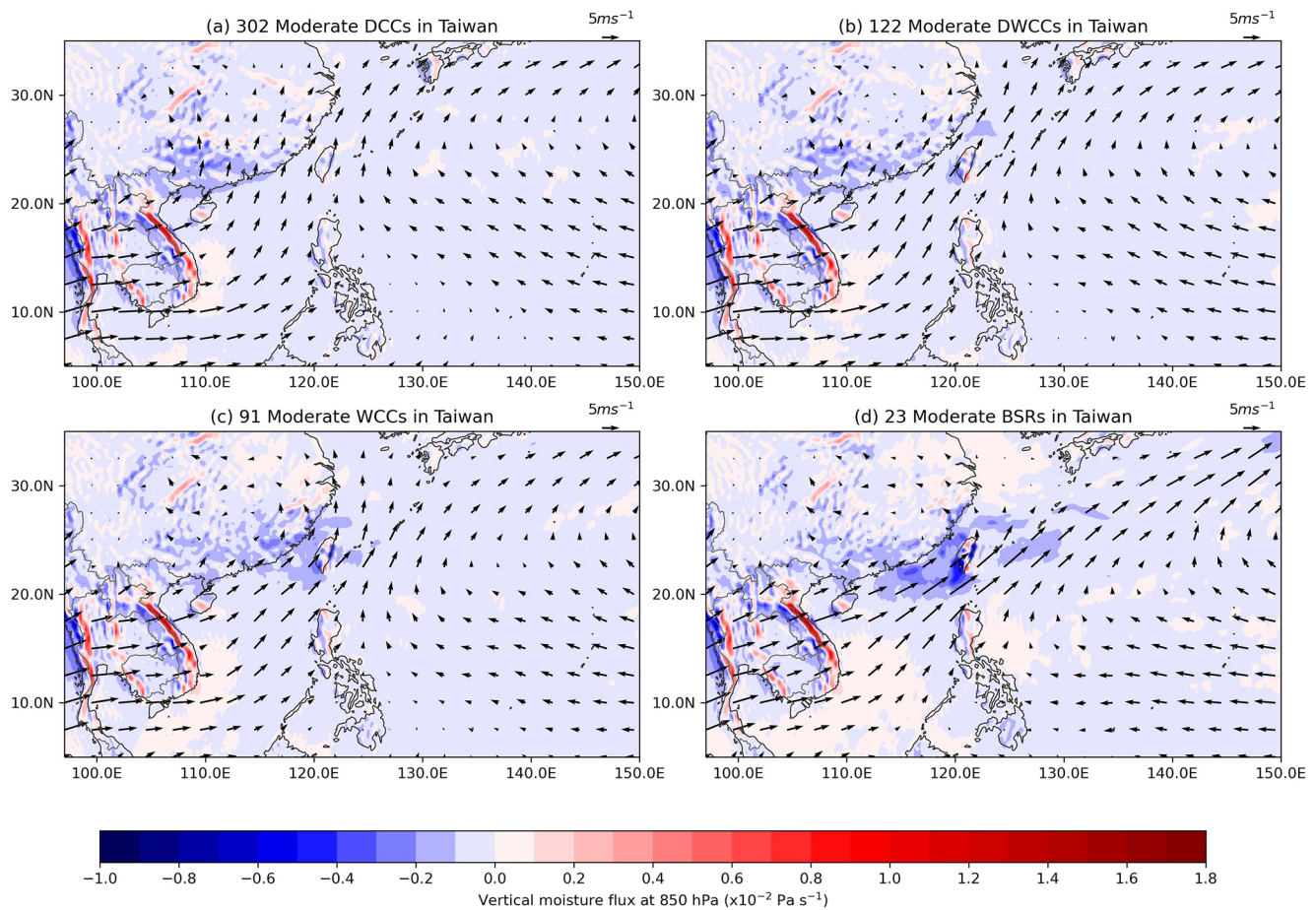
Figure 11. Composite maps of vertical moisture flux (filled) and 850 hPa horizontal wind (vector) on the day the storms were observed by the Tropical Rainfall Measuring Mission satellite during May–September.

located in the central Pacific Ocean centering at 20°N associated with the subtropical high region. Figure 12a shows the moisture divergence composite for the DCCs over the Taiwan subregion. Similar to its counterpart in ωq flux (Figure 11), the negative VIMD over the Taiwan subregion is small in both magnitude and horizontal coverage, indicating that larger-scale forcing is not the only possible source of moisture for DCCs over Taiwan. However, the limitation of the resolution of ERA5 on the local-scale forcing still holds.

The moisture convergence for DWCCs in Taiwan (Figure 12b) is stronger in magnitude and covers a larger area than during the DCC days (Figure 12a). The VIMD composite for the WCCs over Taiwan (Figure 12c) shows broader and larger moisture convergence over the Taiwan subregion relative to the two deep convective categories. This negative region broadens and connects with the Southeast China and the Philippines regions, similar to its ωq flux counterpart (Figure 11c). The moisture convergence pattern off the west coast of Indochina is also larger in magnitude than that in the DCC and DWCC composite.

Figure 12d shows the VIMD composite for BSRs over the Taiwan subregion. Clearly defined moisture divergence regions are notably stronger relative to the other storm types, especially off the west coast of Indochina and over the north coast of China where it broadens. The moisture convergence over Taiwan is the strongest of any storm type shown here and connects with the south of China and spreads further west to the Pacific along 20°–30°N. Moisture convergence corresponds to the upward ωq flux over the same region (Figure 11d), but covers a larger horizontal area especially in the zonal direction.

Comparing Figures 11 and 12, regions with upward ωq flux generally also have vertically integrated moisture convergence, and regions with downward ωq flux generally also have VIMD. Over the Taiwan subregion, the broader and longer-lived storms require stronger and larger-scale upward ωq flux and moisture convergence,
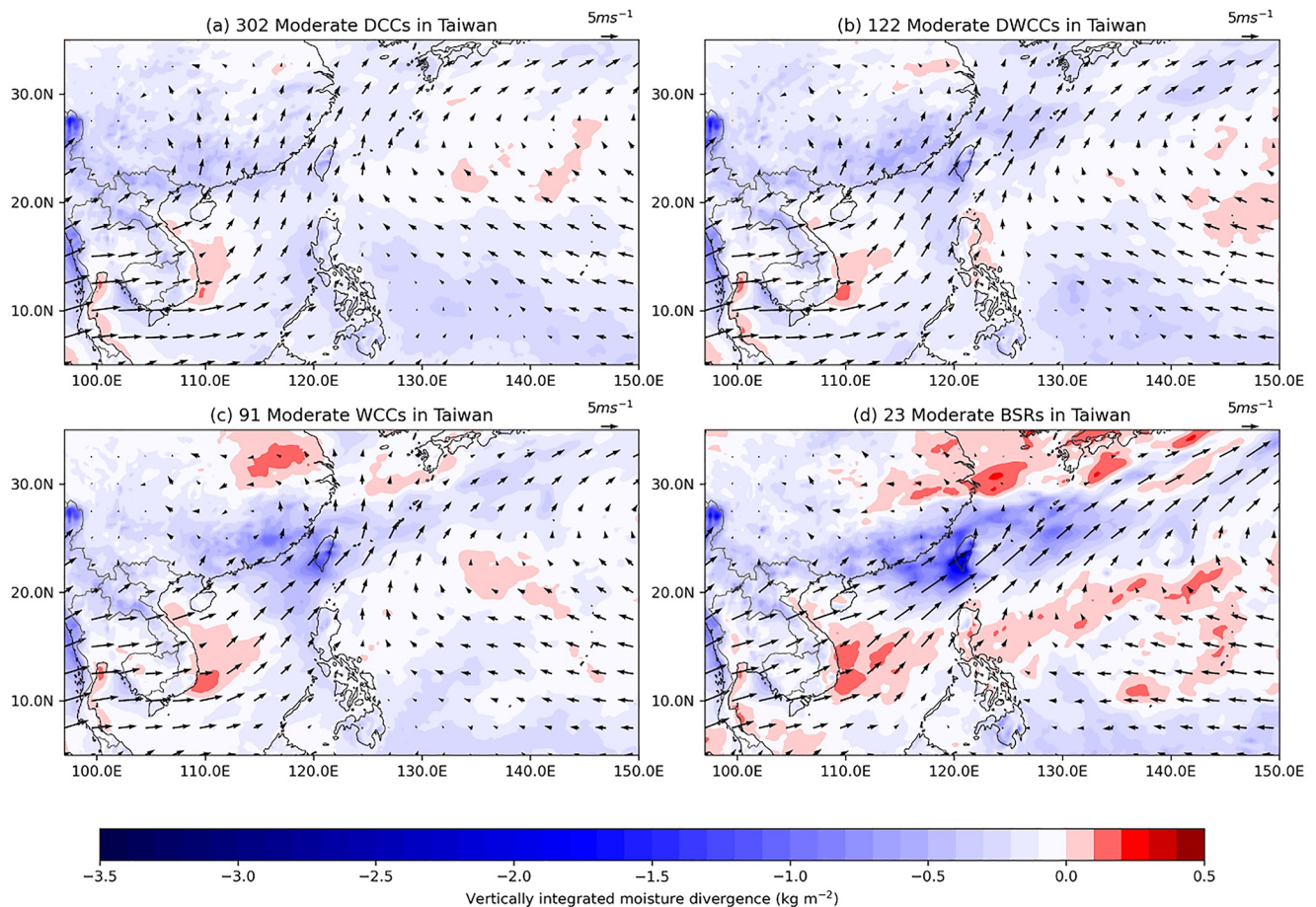
Figure 12. Same as Figure 11, but for vertically integrated moisture divergence (filled) and 850 hPa wind (vector).

which is supported by the mid-level southwesterly flow over the South China Sea carrying the moisture toward the Taiwan subregion.

One of the most prominent phenomena in the TSEA region during the monsoon season is the Meiyu front. To investigate the relationship between the Meiyu front and each extreme echo type, we use LLS to estimate the location of the Meiyu front on the day the extreme echo occurred. Figure 13 shows the daily mean composite of the magnitude and direction of 700–900 hPa LLS. The tropical environment of TSEA shows weak LLS, especially over the Pacific ocean and other regions without terrain. Over land, high LLS induced by the mountains is clear, as seen over the north of Indochina that connects with the Himalayan range to the west. The strong westerly LLS band extending east from China to the Pacific Ocean marks the location of the Meiyu front (Akiyama, 1973; Sampe & Xie, 2010).

Figure 13a shows the LLS composite for days when DCCs occurred over the Taiwan subregion. The LLS band is located near the northern border of the TSEA region. As the Meiyu front moves northward from May to July and is directly over Taiwan in the first half of June (Wu et al., 2017), the location of the LLS region in Figure 13a indicates that the peak environment for DCCs in Taiwan is after the first half of June, consistent with Taiwan DCCs peaking in July (Figure 3a). The Meiyu front is generally located to the north of Taiwan and does not directly affect the environment supporting DCCs over the Taiwan subregion. However, there is moderate LLS over Taiwan, possibly due to orographic effects. This local LLS is not strong or broad in horizontal area, indicating that DCCs do not require a strong mesoscale or larger shear environment and are likely more local in scale, consistent with the previous analyses.
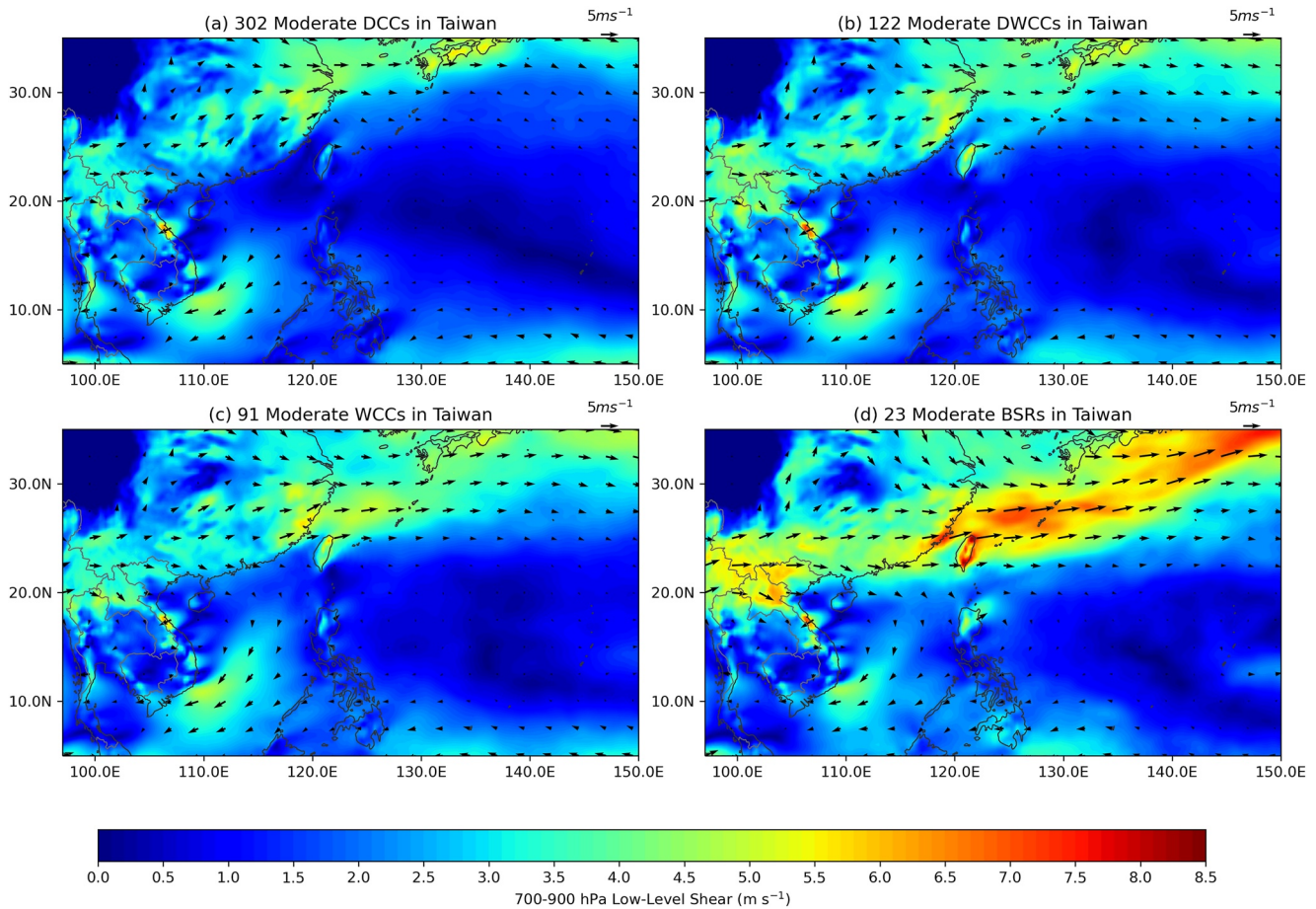
Figure 13. Same as Figure 11, but for 700–900 hPa wind shear magnitude (filled) and direction (vector).

Figure 13b shows a similar LLS pattern for DWCCs compared to DCCs, but with a stronger magnitude. The LLS over Taiwan also extends northeastward and connects with the main Meiyu-front-associated LLS band. This suggests that the LLS environment and season that supports DWCCs is similar to that of DCCs. The stronger LLS composite for DWCCs could be because of two reasons. First, the upscale organization of DWCCs benefits from the stronger shear environment supporting the development of MCSs (LeMone et al., 1998). This would explain the monthly occurrence of DWCCs peaking a month earlier than that of DCCs in the other northern subregions (Figure 3) due to the higher LLS in the environment from proximity of the Meiyu front, which moves north through the summer months. Second, the number of DWCCs is smaller than that of DCCs, so the composite of DCCs has higher variability among the cases and the final composite is not as strong as the composite for DWCCs.

The LLS composite for WCCs shows the strong westerly LLS band located closer to Taiwan (Figure 13c) compared to the DCC and DWCC composites (Figures 13a and 13b). The presence of the Meiyu front located further south indicates that WCCs tend to occur earlier in the monsoon season, consistent with the WCC monthly occurrence distribution (Figure 3c). Strong LLS located near the Taiwan subregion should help support the organization of MCSs over the region, benefiting the development of WCCs. The extra LLS from the Meiyu front may also support the stronger development and reflectivity of WCCs in the northern subregion than the southern region counterpart (Figure 9).

The LLS composite for BSRs (Figure 13d) shows an even stronger westerly LLS band located directly over Taiwan with a maximum magnitude of 9 m/s over the southeast coast of China. Such a strong mesoscale LLS environment over the Taiwan subregion supports the development of long-lived and larger storm systems, such as BSRs over the subregion. Strong LLS is known to support the organization of convections into MCSs (LeMone
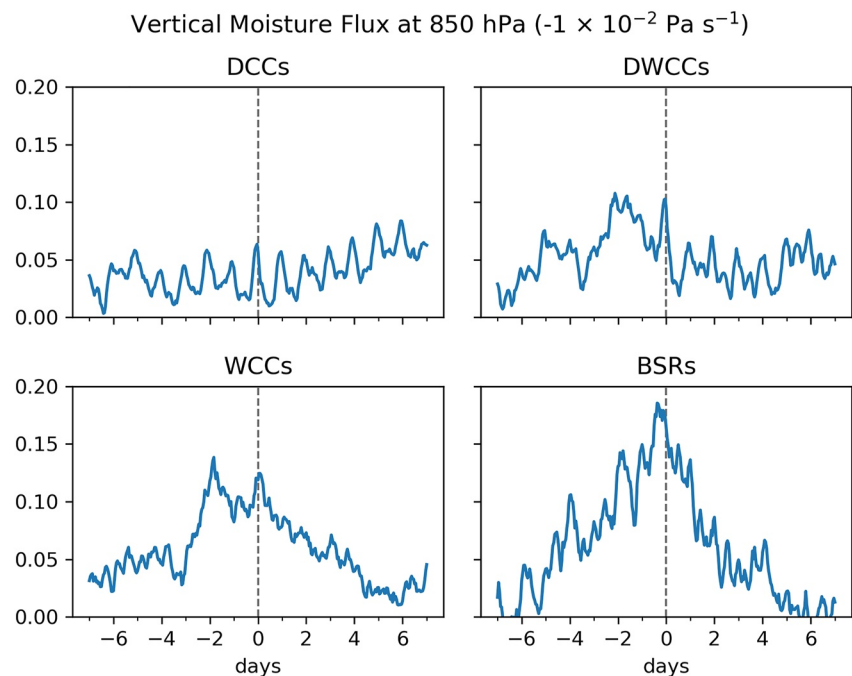
Figure 14. Time-lags of vertical moisture flux at 850 hPa 7 days before and after the storms were observed by the Tropical Rainfall Measuring Mission satellite during May–September.

et al., 1998; Rotunno et al., 1988; Weisman & Rotunno, 2004). The furthest southward location of the Meiyu front corresponds with the early occurrence of BSRs that peak in May (Figure 3d).

As the high westerly LLS band marks the location of the Meiyu front, the LLS composite shows that as the Meiyu front moves across the Taiwan subregion northward, the likelihood of observing extreme storms also shifts from BSRs and WCCs to DWCCs and DCCs, consistent with the monthly occurrence distributions (Figure 3). The stronger mesoscale LLS that accompanies the Meiyu front also helps support the organization of larger MCSs like BSRs. However, the role of smaller-scale LLS on smaller MCSs, that is, DCCs, is not notable in this analysis possibly due to the resolution of ERA5.

4.2. Time-Lagged Composite Analysis of Heavy Rainfall Ingredients

To explore the different time scales of the synoptic and mesoscale factors that vary before and after each extreme echo type over Taiwan, time-lagged hourly averaged ωq flux and LLS over the Taiwan subregion are shown in Figures 14 and 15. The VIMD time-lag analysis is omitted due to its similarity to ωq flux time-lag. The hourly average is computed over 2 weeks centered on the time that the echoes were observed to investigate how the ingredients change over this longer time scale to partially address the duration aspect of the ingredients-based framework (Equation 1).

Significant differences in how the ingredients vary both before and after the occurrence of the TRMM-observed echo at Day 0 are apparent in Figure 14. The build-up and dissipation of ωq flux varies from a notable diurnal cycle in DCCs (Figure 14a) to over a week-long cycle in BSRs (Figure 14d). This time scale variability coincides with the length scale of the upward ωq flux over the Taiwan region (Figure 11) and connects to the ingredients-based equation through the duration term (Equation 1). To illustrate, BSRs often have large-scale moisture supplied from the Meiyu front converging the moisture over Taiwan (Figures 11–13d), and the buildup of moisture in that large-scale perspective is reflected in the week-long build-up and dissipation of ωq flux (Figure 14d).

A shorter time scale of ωq flux is shown in DWCCs and WCCs, which show 2–3 days build-up of ωq flux and up to a week of dissipation after the echoes were observed (Figures 14b and 14c). This is consistent with meso- and larger-scale ωq flux on the day the echoes were observed (Figures 11b and 11c). The composite of LLS also
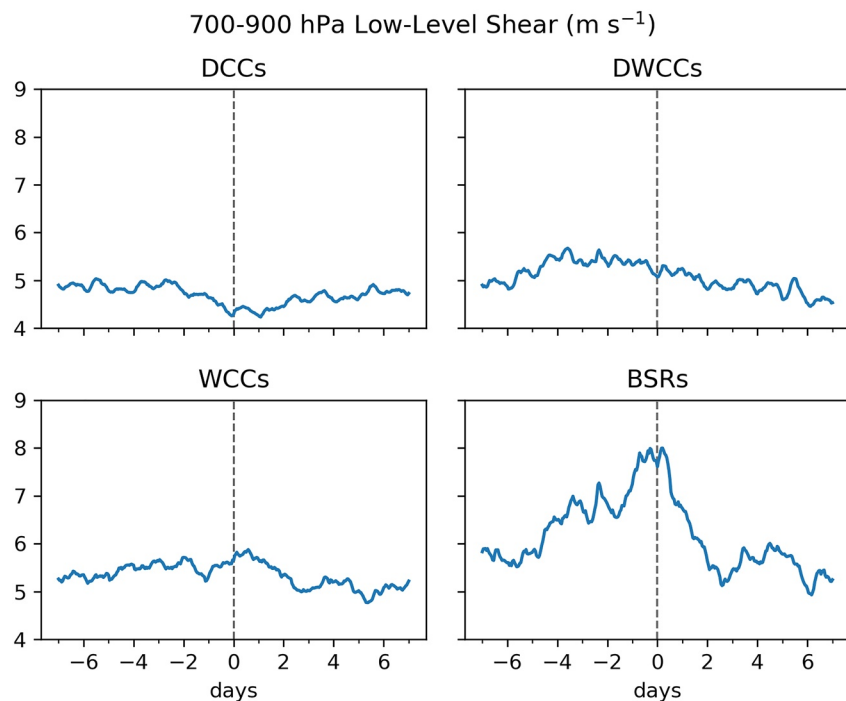
Figure 15. Same as Figure 14, but for 700–900 hPa wind shear.

suggests that the Meiyu front was still close to the north of Taiwan (Figures 13b and 13c) and may be the reason for moisture convergence in the area (Figures 12b and 12c), allowing for the longer time scale of moisture to influence the development of storms with a wide component. However, DWCCs occur most frequently from 5 to 9a.m UTC or 1 to 5p.m Taipei standard time in the analysis of the diurnal cycle (not shown). Thus, the DWCCs are of afternoon storm in nature that develop into larger convective storms. WCCs and BSRs do not show significant diurnal cycle distribution.

On the other hand, DCCs exhibit a clear diurnal cycle associated with the ωq flux that corresponds to the relatively weak pattern of ωq flux over Taiwan (Figure 11a), suggesting a more local phenomena. Diurnally driven afternoon thunderstorms in the Taipei basin have been shown to produce significant rainfall and flooding in the region (Kerns et al., 2010; Lin et al., 2011). Analysis of the diurnal cycle of the extreme echoes shows that DCCs and DWCCs occur most frequently in the afternoon from 4 to 9 UTC or 12 to 5pm Taipei standard time (not shown). It is likely that afternoon storms are a primary type of event corresponding to DCCs and DWCCs. WCCs and BSRs shows weaker diurnal cycle, peaking earlier in the day from 5 to 10am and 11am to 1pm Taipei standard time, respectively (also not shown). The diurnal cycle signal might not show clearly in the time-lag analysis (Figures 14 and 15) due to the stronger influence of longer-timescale signal. Nonetheless, the diurnal cycle signal found is consistent with prior research of DCCs, WCCs, DWCCs, and BSRs (Zuluaga & Houze, 2013).

The hourly average of 700–900 hPa LLS over the Taiwan subregion shows a similar build-up and dissipation time scale to the ωq flux composite (Figures 14 and 15). The weeklong buildup of LLS for BSRs is pronounced (Figure 15d), showing the influence of the Meiyu front slowly moving over the Taiwan region (Figure 13d). The week-long build-up of LLS coincides with the week-long build-up of the ωq flux (Figure 14d), further supporting the hypothesis that the Meiyu front converges the moisture to the region associated with BSRs.

The build-up of LLS is weaker but still apparent for DWCCs and WCCs (Figures 15b and 15c), showing that the Meiyu front likely influences these storm types, but not as strongly as BSRs. The build-up complements the composite map of LLS that the Meiyu front location is to the north of Taiwan and not directly over the Taiwan region like BSRs (Figures 13b–13d).

Lastly, the average LLS is very weak for DCCs the week before and after DCCs were observed by TRMM (Figure 15a), coinciding with the weak and small spatial scale of the signal of LLS (Figure 13a). This reinforces

the hypothesis that large-scale LLS or large-scale moisture convergence from the Meiyu front is not a primary factor for DCC development. However, it does not discount the effect of ERA5 resolution on the results related to the smaller-scale storm environments.

Thus, the broader storms require stronger meso- and larger scale LLS and ωq flux to support the large-scale development and organization, associated with large-scale phenomena in the vicinity of Taiwan—that is, the Meiyu front and the East Asian monsoon. In contrast, smaller storms like DCCs are associated with weaker LLS and ωq flux on the synoptic scale without a longer time scale buildup. The diurnal cycle is apparent in ωq flux especially in DCCs, in which the impacts of afternoon heating on storm occurrence is pronounced.

5. Conclusions

In this study, we analyze the climatology of storms with extreme horizontal and vertical dimensions related to heavy rainfall observed by the TRMM satellite's PR from 1998 to 2013 over the TSEA region, which is a high moisture environment affected by the West Pacific warm pool and the East Asian monsoon.

The climatology over TSEA shows that DCCs and DWCCs have a higher probability to occur over the land than the sea environments. On the other hand, WCCs and BSRs are more likely to occur over the seas. DCCs and DWCCs share similar monthly occurrence distributions, peaking in the late monsoon season in the northern subregions (i.e., the North Pacific, Southeast China, and Taiwan), and in early monsoon season in the southern subregions (i.e., Indochina, South China Sea, the Philippines, and the Philippines Sea). However, the WCCs occur early in the monsoon season for the northern subregions in association with the local spring rain season and later in the season for the southern subregions in association with the maritime-continent monsoon. BSRs monthly occurrence distributions differ from the convective categories, suggesting different environments that may support the storms. The BSRs in the northern subregions are strongly associated with the East Asian monsoon and the Meiyu front at the onset of the monsoon.

The CFAD analysis shows the DCCs and the DWCCs have similar strong high-reflectivity in low-level and low-reflectivity, with land-and-sea variability in structure. The WCCs structure is weaker and varies depending on whether they occur over north or south subregions. The BSRs structure also reflects north-south subregions differences, and a stronger bright band over the southern subregion.

DCCs and DWCCs produce a higher rain rate when occurring over the land environments and have different storm structures over land and sea subregions, possibly due to the orographic lifting and coastal effects. Together, they contribute to the highest rain rates observed over TSEA. However, due to the small area DCCs contribute small volumetric rain rates across the TSEA region. WCCs and DWCCs contribute slightly larger volumetric rain rates due to broader horizontal areas. BSRs produce the lowest mean rain rates among the extreme echo categories, but ultimately contribute the largest volumetric rain thanks to the broad horizontal areas and long duration.

The ingredients-based analysis over the Taiwan subregion shows that the larger systems (i.e., WCCs and BSRs) have broader areas and longer-timescale buildup of ωq flux and moisture convergence over the region of interest (i.e., Taiwan), implying that they require mesoscale or larger-scale moisture and vertical motion to support their development. On the other hand, the smaller, more vigorous systems (i.e., DCCs) only have weak, small areas of ωq flux and moisture convergence near Taiwan in the reanalysis data. The time-lagged analysis also shows a smaller-amplitude diurnal cycle of the ωq flux. However, we cannot conclude that the DCCs do not require stronger vertical moisture flux due to the ERA5 resolution limitation.

In contrast, when broader systems occur near Taiwan (i.e., WCCs and BSRs), a broad area of LLS is over the region and a week-long timescale buildup of LLS prior to the event, suggesting that the broader systems require mesoscale or larger LLS to support the development of broader, more organized systems. The prominent LLS contributor is the Meiyu front, which comes at the onset of the East Asian monsoon corresponding to the WCCs and BSRs monthly occurrence distributions.

Across TSEA regions, storm and rain characteristics shows that diverse environments of TSEA contribute to various storm structures and distributions, as shown in the differences between land and sea subregions, and north and south subregions. These variations suggest that there are many dynamics or phenomena playing the role in the production of extreme rainfall in the region. Over the Taiwan subregion, the Meiyu front is a key phenomenon

that brings large-scale ingredients favorable for extreme storm development and sustenance over large regions and long periods of time. However, because of the limitation of the ERA5 resolution, we cannot draw conclusion about storm-scale ingredients.

Future work will include using higher resolution datasets, both from observations and model simulations, to further analyze the relationship between extreme storms in the TSEA region and the ingredients that support heavy rainfall. Comparisons between observations from the recently conducted PRECIP field campaign in Taiwan and Yonaguni Island (May–August 2022) and the TRMM climatology from this paper would be of interest to further explore the convective through mesoscale perspectives of the ingredients-based framework in a moisture-rich environment. Enhanced understanding of how specific storm modes relate to heavy rainfall in a moisture-rich environment provides important information on the ingredients supporting such high-impact events, the relevant physical processes, and global implications for the production of heavy rainfall in moisture-rich and moisture-limited environments globally.

Data Availability Statement

TRMM PR data used for this study is available at (Houze et al., 2015a) and supported by the NASA Earth Sciences Precipitation Measurement Missions Program. ERA5 data used for this study is available at (Copernicus Climate Change Service (C3S), 2017).

References

Akiyama, T. (1973). The large-scale aspects of the characteristic features of the Baiu front. *Papers in Meteorology and Geophysics*, *24*(2), 157–188. https://doi.org/10.2467/mripapers1950.24.2_157

Ashley, S. T., & Ashley, W. S. (2008). Flood fatalities in the United States. *Journal of Applied Meteorology and Climatology*, *47*(3), 805–818. https://doi.org/10.1175/2007JAMC1611.1

Awaka, J., Iguchi, T., Kumagai, H., & Okamoto, K. (1997). Rain type classification algorithm for TRMM precipitation radar. In *IGARSS'97. 1997 IEEE international geoscience and remote sensing symposium proceedings* (Vol. 4, pp. 1633–1635). Remote Sensing—A Scientific Vision for Sustainable Development. https://doi.org/10.1109/IGARSS.1997.608993

Brauer, N. S., Basara, J. B., Homeyer, C. R., McFarquhar, G. M., & Kirstetter, P. E. (2020). Quantifying precipitation efficiency and drivers of excessive precipitation in post-landfall hurricane Harvey. *Journal of Hydrometeorology*, *21*(3), 433–452. https://doi.org/10.1175/JHM-D-19-0192.1

Brown, P. J., Kummerow, C. D., & Randel, D. L. (2016). Hurricane GPROF: An optimized ocean microwave rainfall retrieval for tropical cyclones. *Journal of Atmospheric and Oceanic Technology*, *33*(7), 1539–1556. https://doi.org/10.1175/JTECH-D-15-0234.1

Chang, C.-P., Wang, Z., McBride, J., & Liu, C.-H. (2005). Annual cycle of southeast Asia—Maritime continent rainfall and the asymmetric monsoon transition. *Journal of Climate*, *18*(2), 287–301. https://doi.org/10.1175/JCLI-3257.1

Chen, C.-S., & Chen, Y.-L. (2003). The rainfall characteristics of Taiwan. *Monthly Weather Review*, *131*(7), 1323–1341. https://doi.org/10.1175/1520-0493(2003)131<1323:trcot>2.0.co;2

Chen, C.-S., Chen, Y.-L., Liu, C.-L., Lin, P.-L., & Chen, W.-C. (2007). Statistics of heavy rainfall occurrences in Taiwan. *Weather and Forecasting*, *22*(5), 981–1002. https://doi.org/10.1175/WAF1033.1

Chen, S. S., Houze, R. A., & Mapes, B. E. (1996). Multiscale variability of deep convection in realation to large-scale circulation in TOGA COARE. *Journal of the Atmospheric Sciences*, *53*(10), 1380–1409. https://doi.org/10.1175/1520-0469(1996)053<1380:MVODCI>2.0.CO;2

Copernicus Climate Change Service (C3S). (2017). ERA5: Fifth generation of ECMWF atmospheric reanalyses of the global climate [Dataset]. Chang. Retrieved from https://www.ecmwf.int/en/forecasts/datasets/reanalysis-datasets/era5

DeHart, J. C., & Bell, M. M. (2020). A comparison of the polarimetric radar characteristics of heavy rainfall from Hurricanes Harvey (2017) and Florence (2018). *Journal of Geophysical Research: Atmospheres*, *125*(11), e2019JD032212. https://doi.org/10.1029/2019JD032212

Ding, Y. (1992). Summer monsoon rainfalls in China. *Journal of the Meteorological Society of Japan. Ser. II*, *70*(1B), 373–396. https://doi.org/10.2151/jmsj1965.70.1B_373

Ding, Y., & Chan, J. C. L. (2005). The East Asian summer monsoon: An overview. *Meteorology and Atmospheric Physics*, *89*(1–4), 117–142. https://doi.org/10.1007/s00703-005-0125-z

Doswell, C., Brooks, H., & Maddox, R. A. (1996). Flash flood forecasting: An ingredients-based methodology. *Weather and Forecasting*, *11*(4), 560–581. https://doi.org/10.1175/1520-0434(1996)011<0560:fffaib>2.0.co;2

Dougherty, E., & Rasmussen, K. L. (2020). Changes in future flash flood–producing storms in the United States. *Journal of Hydrometeorology*, *21*(10), 2221–2236. https://doi.org/10.1175/JHM-D-20-0014.1

Dougherty, E., & Rasmussen, K. L. (2021). Variations in flash flood-producing storm characteristics associated with changes in vertical velocity in a future climate in the Mississippi River Basin. *Journal of Hydrometeorology*, *22*(3), 671–687. https://doi.org/10.1175/jhm-d-20-0254.1

Gingrey, A., Varble, A., & Zipser, E. (2018). Relationships between extreme rain rates and convective intensities from the perspectives of TRMM and WSR-88D radars. *Journal of Applied Meteorology and Climatology*, *57*(6), 1353–1369. https://doi.org/10.1175/JAMC-D-17-0240.1

Gochis, D., Schumacher, R., Friedrich, K., Doesken, N., Kelsch, M., Sun, J., et al. (2015). The great Colorado flood of September 2013. *Bulletin of the American Meteorological Society*, *96*(9), 1461–1487. https://doi.org/10.1175/BAMS-D-13-00241.1

Gutmann, E. D., Rasmussen, R. M., Liu, C., Ikeda, K., Bruyere, C. L., Done, J. M., et al. (2018). Changes in Hurricanes from a 13-Yr convection-permitting pseudo–global warming simulation. *Journal of Climate*, *31*(9), 3643–3657. https://doi.org/10.1175/JCLI-D-17-0391.1

Hamada, A., Murayama, Y., & Takayabu, Y. N. (2014). Regional characteristics of extreme rainfall extracted from TRMM PR measurements. *Journal of Climate*, *27*(21), 8151–8169. https://doi.org/10.1175/JCLI-D-14-00107.1

Henny, L., Thorncroft, C. D., Hsu, H.-H., & Bosart, L. F. (2021). Extreme rainfall in Taiwan: Seasonal statistics and trends. *Journal of Climate*, *34*(12), 4711–4731. https://doi.org/10.1175/JCLI-D-20-0999.1

Houze, R. A., Chen, S. S., Kingsmill, D. E., Serra, Y., & Yuter, S. E. (2000). Convection over the Pacific warm pool in relation to the atmospheric Kelvin-Rossby wave. *Journal of the Atmospheric Sciences*, *57*(18), 3058–3089. https://doi.org/10.1175/1520-0469(2000)057<3058:cotpwp>2.0.co;2

Houze, R. A., Rasmussen, K. L., Medina, S., Brodzik, S. R., & Romatschke, U. (2011). Anomalous atmospheric events leading to the summer 2010 floods in Pakistan. *Bulletin of the American Meteorological Society*, *92*(3), 291–298. https://doi.org/10.1175/2010BAMS3173.1

Houze, R. A., Rasmussen, K. L., Zuluaga, M. D., & Brodzik, S. R. (2015a). University of Washington TRMM data set [Dataset]. University of Washington. Retrieved from http://trmm.atmos.washington.edu/

Houze, R. A., Rasmussen, K. L., Zuluaga, M. D., & Brodzik, S. R. (2015b). The variable nature of convection in the tropics and subtropics: A legacy of coper of the tropical rainfall measuring mission satellite. *Reviews of Geophysics*, *53*(3), 994–1021. https://doi.org/10.1002/2015RG000488

Houze, R. A., Wilton, D. C., & Smull, B. F. (2007). Monsoon convection in the Himalayan region as seen by the TRMM precipitation radar. *Quarterly Journal of the Royal Meteorological Society*, *133*, 1389–1411. https://doi.org/10.1002/qj

Hung, C.-W., Hsu, H.-H., & Lu, M.-M. (2004). Decadal oscillation of spring rain in northern Taiwan. *Geophysical Research Letters*, *31*(22), L22206. https://doi.org/10.1029/2004GL021344

Iguchi, T., Kozu, T., Kwiatkowski, J., Meneghini, R., Awaka, J., & Okamoto, K. (2009). Uncertainties in the rain profiling algorithm for the TRMM precipitation radar. *Journal of the Meteorological Society of Japan. Ser. II*, *87A*, 1–30. https://doi.org/10.2151/jmsj.87A.1

Iguchi, T., Kozu, T., Meneghini, R., Awaka, J., & Okamoto, K. (2000). Rain-profiling algorithm for the TRMM precipitation radar. *Journal of Applied Meteorology and Climatology*, *39*(12), 2038–2052. https://doi.org/10.1175/1520-0450(2001)040<2038:rpaftt>2.0.co;2

Iguchi, T., Meneghini, R., Awaka, J., Kozu, T., & Okamoto, K. (2000). Rain profiling algorithm for TRMM precipitation radar data. *Advances in Space Research*, *25*(5), 973–976. https://doi.org/10.1016/S0273-1177(99)00933-3

Kerns, B. W. J., Chen, Y.-L., & Chang, M.-Y. (2010). The diurnal cycle of winds, rain, and clouds over Taiwan during the Mei-Yu, summer, and autumn rainfall regimes. *Monthly Weather Review*, *138*(2), 497–516. https://doi.org/10.1175/2009MWR3031.1

Klotzbach, P. P., Bowen, S. G., PielKe, R. G. R., & Bell, M. (2018). Continental U.S. hurricane landfall frequency and associated damage: Observations and future risks. *Bulletin of the American Meteorological Society*, *99*(7), 1359–1376. https://doi.org/10.1175/BAMS-D-17-0184.1

Knutson, T., Camargo, S. J., Chan, J. C. L., Emanuel, K., Ho, C.-H., Kossin, J., et al. (2020). Tropical cyclones and climate change assessment: Part II: Projected response to anthropogenic warming. *Bulletin of the American Meteorological Society*, *101*(3), E303–E322. https://doi.org/10.1175/BAMS-D-18-0194.1

Lau, K., & Yang, S. (1997). Climatology and interannual variability of the Southeast Asian summer monsoon. *Advances in Atmospheric Sciences*, *14*(2), 141–162. https://doi.org/10.1007/s00376-997-0016-y

LeMone, M. A., Zipser, E. J., & Trier, S. B. (1998). The role of environmental shear and thermodynamic conditions in determining the structure and evolution of mesoscale convective systems during TOGA COARE. *Journal of the Atmospheric Sciences*, *55*(23), 3493–3517. https://doi.org/10.1175/1520-0469(1998)055⟨3493:troesa⟩2.0.co;2

Leslie, J. (2019). U.S. has its wettest 12 months on record—again National Oceanic and Atmospheric Administration. Retrieved from https://www.noaa.gov/news/us-has-its-wettest-12-months-on-record-again

Lin, P.-F., Chang, P.-L., Jou, B. J.-D., Wilson, J. W., & Roberts, R. D. (2011). Warm season afternoon thunderstorm characteristics under weak synoptic-scale forcing over Taiwan Island. *Weather and Forecasting*, *26*(1), 44–60. https://doi.org/10.1175/2010WAF2222386.1

LinHo, L. H., Huang, X., & Lau, N.-C. (2008). Winter-to-Spring transition in East Asia: A planetary-scale perspective of the South China spring rain onset. *Journal of Climate*, *21*(13), 3081–3096. https://doi.org/10.1175/2007JCLI1611.1

Ninomiya, K., & Shibagaki, Y. (2007). Multi-scale features of the Meiyu-Baiu front and associated precipitation systems. *Journal of the Meteorological Society of Japan*, *85B*, 103–122. https://doi.org/10.2151/jmsj.85B.103

Nugent, A. D., Longman, R. J., Trauernicht, C., Lucas, M. P., Diaz, H. F., & Giambelluca, T. W. (2020). Fire and rain: The legacy of hurricane lane in Hawai'i. *Bulletin of the American Meteorological Society*, *101*(6), E954–E967. https://doi.org/10.1175/BAMS-D-19-0104.1

Rasmussen, K. L., Choi, S. L., Zuluaga, M. D., & Houze, R. A. (2013). TRMM precipitation bias in extreme storms in South America. *Geophysical Research Letters*, *40*(13), 3457–3461. https://doi.org/10.1002/grl.50651

Rasmussen, K. L., Hill, A. J., Toma, V. E., Zuluaga, M. D., Webster, P. J., & Houze, R. A. (2015). Multiscale analysis of three consecutive years of anomalous flooding in Pakistan. *Quarterly Journal of the Royal Meteorological Society*, *141*(689), 1259–1276. https://doi.org/10.1002/qj.2433

Rasmussen, K. L., & Houze, R. A. (2011). Orogenic convection in subtropical South America as seen by the TRMM satellite. *Monthly Weather Review*, *139*(8), 2399–2420. https://doi.org/10.1175/MWR-D-10-05006.1

Rasmussen, K. L., & Houze, R. A. (2012). A flash-flooding storm at the steep edge of high terrain: Disaster in the Himalayas. *Bulletin of the American Meteorological Society*, *93*(11), 1713–1724. https://doi.org/10.1175/BAMS-D-11-00236.1

Rasmussen, K. L., & Houze, R. A. (2016). Convective initiation near the Andes in subtropical South America. *Monthly Weather Review*, *144*(6), 2351–2374. https://doi.org/10.1175/MWR-D-15-0058.1

Rasmussen, K. L., Zuluaga, M. D., & Houze, R. A. (2014). Severe convection and lightning in subtropical South America. *Geophysical Research Letters*, *41*(20), 7359–7366. https://doi.org/10.1002/2014GL061767

Romatschke, U., & Houze, R. A. (2011). Characteristics of precipitating convective systems in the South Asian monsoon. *Journal of Hydrometeorology*, *12*(1), 3–26. https://doi.org/10.1175/2010JHM1289.1

Romatschke, U., Medina, S., & Houze, R. A. (2010). Regional, seasonal, and diurnal variations of extreme convection in the South Asian region. *Journal of Climate*, *23*(2), 419–439. https://doi.org/10.1175/2009JCLI3140.1

Rotunno, R., Klemp, J. B., & Weisman, M. L. (1988). A theory for strong, long-lived squall lines. *Journal of the Atmospheric Sciences*, *45*(3), 463–485. https://doi.org/10.1175/1520-0469(1988)045<0463:atfsll>2.0.co;2

Sampe, T., & Xie, S. P. (2010). Large-scale dynamics of the Meiyu-Baiu rainband: Environmental forcing by the westerly jet. *Journal of Climate*, *23*(1), 113–134. https://doi.org/10.1175/2009JCLI3128.1

Sukovich, E. M., Ralph, F. M., Barthold, F. E., Reynolds, D. W., & Novak, D. R. (2014). Extreme quantitative precipitation forecast performance at the weather prediction center from 2001 to 2011. *Weather and Forecasting*, *29*(4), 894–911. https://doi.org/10.1175/WAF-D-13-00061.1

Trenberth, K. E., Stepaniak, D. P., & Caron, J. M. (2000). The global monsoon as seen through the divergent atmospheric circulation. *Journal of Climate*, *13*(22), 3969–3993. https://doi.org/10.1175/1520-0442(2000)013<3969:tgmast>2.0.co;2

Ulbrich, C. W., & Atlas, D. (2002). On the separation of tropical convective and stratiform rains. *Journal of Applied Meteorology and Climatology*, *41*(2), 188–195. https://doi.org/10.1175/1520-0450(2002)041<0188:otsotc>2.0.co;2

Weisman, M. L., & Rotunno, R. (2004). "A theory for strong long-lived squall lines" revisited. *Journal of the Atmospheric Sciences*, *61*(4), 361–382. https://doi.org/10.1175/1520-0469(2004)061<0361:atfsls>2.0.co;2

Wu, M., Wu, C.-C., Yen, T.-H., & Luo, Y. (2017). Synoptic analysis of extreme hourly precipitation in Taiwan during 2003–12. *Monthly Weather Review*, *145*(12), 5123–5140. https://doi.org/10.1175/MWR-D-17-0230.1

Yu, H., Rasmussen, K. L., & Kuo, H.-C. (2021). Quasi-2-Day and diurnal cloud variation timescales over convectively active regions. *Journal of Geophysical Research: Atmospheres*, *126*(21), e2021JD035426. https://doi.org/10.1029/2021JD035426

Yuter, S. E., & Houze, R. A. (1995). Three-dimensional kinematic and microphysical evolution of Florida cumulonimbus. Part II: Frequency distributions of vertical velocity, reflectivity, and differential reflectivity. *Monthly Weather Review*, *123*(7), 1941–1963. https://doi.org/10.1175/1520-0493(1995)123<1941:tdkame>2.0.co;2

Zipser, E. J., Cecil, D. J., Liu, C., Nesbitt, S. W., & Yorty, D. P. (2006). Where are the most intense thunderstorms on Earth? *Bulletin of the American Meteorological Society*, *87*(8), 1057–1072. https://doi.org/10.1175/BAMS-87-8-1057

Zuluaga, M. D., & Houze, R. A. (2013). Evolution of the population of precipitating convective systems over the equatorial Indian ocean in active phases of the Madden–Julian oscillation. *Journal of the Atmospheric Sciences*, *70*(9), 2713–2725. https://doi.org/10.1175/JAS-D-12-0311.1